Magnetization relaxation dynamics in [Co/Pt]₃ multilayers on pico- and nanosecond timescales

Fangzhou Wang [1,*] Daniel E. Bürgler [1], Roman Adam,[1] Umut Parlak [1], Derang Cao,[1,2] Christian Greb [1],
Sarah Heidtfeld,[1] and Claus M. Schneider[1,3,4]

[1]*Peter Grünberg Institute, Research Centre Jülich, 52425 Jülich, Germany*
[2]*College of Physics, Center for Marine Observation and Communications, Qingdao University, 266071 Qingdao, China*
[3]*Faculty of Physics, University Duisburg-Essen, 47057 Duisburg, Germany*
[4]*Department of Physics, University of California Davis, Davis, California 95616-5270, USA*

We experimentally investigated magnetization relaxation dynamics in the largely unexplored time window extending from few picoseconds up to two nanoseconds following femtosecond laser pulse excitation. We triggered magnetization dynamics in [Co(0.4 nm)/Pt(0.7 nm)]₃ multilayers and measured the resulting magneto-optic response by recording both transient hysteresis loops as well as transients of magnetization dynamics. We observe that the coercive field of the sample is still strongly suppressed even ∼1 ms after the laser excitation, which is three orders of magnitude longer than the recovery time of the magnetization amplitude. In addition, we succeeded to fit the magnetization relaxation data in the entire experimentally observed time window by considering two phenomenological time constants τ_f^* and τ_s^* describing fast (ps) and slow (ns) magnetization relaxation processes, respectively. The fits of the data suggest a magnetic field dependent relaxation slowdown beyond 100 ps after excitation. We observe an explosion of the τ_f^* and τ_s^* values when the magnetization is completely quenched and relaxes intrinsically in the absence of an external magnetic field. We interpret the phenomenological time constants τ_f^* and τ_s^* using an intuitive physical picture based on the Landau-Lifshitz-Bloch model and numerical solutions of the extended three-temperature model [Shim *et al.*, Sci. Rep. **10**, 6355 (2020)].

I. INTRODUCTION

Ultrafast control of the magnetization orientation in ferromagnetic thin films on femto- and picosecond timescales currently attracts strong interest, not only because of its scientific allure, but also for its vast potential to impact future magnetic storage technologies. It has been shown to enable an unprecedented speed of magnetization reversal [1–3] and, possibly, could offer an alternative approach to data processing techniques [4–6]. Understanding the physical processes governing the spin system dynamics is crucial in order to define the speed and efficiency of the switching process. Up to date, optically induced magnetization reversal, also known as all-optical-switching (AOS), has been intensively studied in ferrimagnetic systems, such as GdFeCo and TbCo alloys [7–12], and ferromagnetic [Co/Pt]ₙ multilayers [13–17]. The latter belong to the most thoroughly studied systems, due to a broad range of devices and effects based on this system, such as spin valve devices [18,19], magnetic tunnel junctions (MTJs) [20,21], magnetic random access memories

(MRAMs) [22], skyrmion generation [23], or THz emission [24,25].

Since the magnetization dynamics on the femtosecond timescale is beyond the limits of classical Landau-Lifshitz-Gilbert (LLG) theory, the spin dynamics is often described in the framework of the so-called phenomenological three-temperature model (3TM) [1,26] by tracing the energy flow among the interacting electron, spin, and lattice reservoirs, which are assigned different effective temperatures [2]. Based on the 3TM, Koopmans *et al.* have developed the microscopic three-temperature model (M3TM) model [27] that was successfully applied to numerous experimental observations [14,28–30]. However, both the 3TM and the M3TM seem to describe the experimental data only in a limited time window (<100 ps) [31]. Another approach to analyze ultrafast laser-induced magnetization dynamics is the Landau-Lifshitz-Bloch (LLB) model, which was developed by Garanin in 1997 based on the Fokker-Planck equation [32]. The model distinguishes longitudinal and transverse magnetization relaxation. The former affects the magnetization amplitude, and the latter proceeds via LLG damping of magnetization precession. The LLB model suggests [33] that longitudinal and transverse relaxation can be treated as independent processes and contribute to the magnetization dynamics at different timescales. The LLB model was successfully applied to explain magnetization dynamics in ferromagnetic Ni by Atxitia and co-workers [34,35] resulting in significant agreement between the model and experiments. Interestingly, Atxitia

---

*f.wang@fz-juelich.de

and Chubykalo-Fesenko demonstrated the equivalence of the M3TM and the LLB model, if precessional dynamics is not taken into account in the latter [33].

Magnetization dynamics of ferromagnetic [Co/Pt]$_N$ multilayer systems in the ultrafast time regime have been studied extensively in a large parameter space, such as external field [28], sample structure [14,36,37], laser fluence [28], laser repetition rate [17], or light polarization [38]. It is generally assumed that the observed relaxation dynamics is the consequence of an interplay between several physical mechanisms and the contribution weight of each mechanism may vary depending on the external parameters. Experiments using element-selective soft x-ray probing [39] suggest that the magnetization relaxation processes after optical excitation may be associated with phonon [40] or magnon generation [41] due to the presence of hot electrons. Each of these processes may affect the magnetization dynamics on different timescales [30]. In addition, [Co/Pt]$_N$ multilayers were shown to feature a so-called accumulative switching, where multiple pulses are needed for a complete reversal of the magnetization [13]. The mechanism of the reversal has been related to the inverse Faraday effect (IFE) [42] or to heat-driven magnetic circular dichroism (MCD) [43]. The connection between magnetization switching and relaxation has been addressed within the 3TM. Nevertheless, the role of magnetization relaxation dynamics in this switching process is still unclear and requires further investigation.

In this paper, we present an experimental study on magnetization *relaxation processes* following femtosecond optical excitation of [Co/Pt]$_3$ multilayers examined by the time-resolved polar magneto-optic Kerr effect (TR-P-MOKE). The motivation of the study is to understand spin dynamics in ferromagnetic multilayers that enable spintronic applications in the frequency range from DC (MTJs), through low frequencies (MRAMs), up to 10^{12} Hz (THz generation and AOS). In contrast to most earlier studies that have been focusing on the dynamics in the time window of a few picoseconds [14,28,36], our measurements span the relaxation time window starting from subpicoseconds up to two nanoseconds after the optical excitation. Our analysis reveals the presence of at least two mechanisms that drive the system back to equilibrium. For an in-depth analysis, we fit the transient magnetization curves with a phenomenological response function comprising two phenomenological time constants τ_f^* and τ_s^* describing fast (ps) and slow (ns) magnetization relaxation processes, respectively. We discuss our findings also in the framework of the extended three-temperature model (E3TM) [44] and the extended microscopic three-temperature model (eM3TM) [45]. Finally, we interpret the phenomenological time constants τ_f^* and τ_s^* using an intuitive physical picture based on the LLB model and numerical solutions of the E3TM, which fits our data very well for timescales <200 ps.

II. EXPERIMENTAL PROCEDURES

A. Sample fabrication

[Co(0.4 nm)/Pt(0.7 nm)]$_3$ multilayers were fabricated on top of oxidized Si(001) wafers by magnetron sputtering at room temperature. A 5-nm-thin Ta buffer layer and a

2-nm-thin Pt capping layer were added in order to achieve perpendicular magnetic anisotropy (PMA) and to prevent oxidation, respectively. The deposition rate for each material was monitored by a quartz crystal microbalance. The thickness of the multilayer stack was calibrated by x-ray reflectivity (XRR) measurements. In order to confirm out-of-plane magnetization, we employed static magneto-optic Kerr effect magnetometry in polar geometry (P-MOKE) for measuring the magnetic hysteresis loops.

B. Pump-probe experiments

Our experiments employ a two-color pump-probe configuration with pump and probe beams at 800 and 400 nm wavelength, respectively, both pointed towards the sample surface at near-perpendicular (<5°) incidence. The laser spots of pump and probe at the sample surface were focused with a diameter ratio of 4:1 (240 μm : 60 μm), ensuring perfect spatial overlap and probing of the center of the laser-affected area. After reflection from the sample, the probe light was split by a Wollaston prism into orthogonally polarized beams that were detected using two photodiodes and two lock-in systems synchronized to the 1-kHz laser pulse repetition rate. The TR-P-MOKE signal at each time-delay is obtained as the difference of absolute values of signals measured at two opposite out-of-plane magnetic fields $H^+ > 0$ and $H^- = -H^+$, where the maximum field is $H^+ = 80$ kA/m. As this procedure is expected to subtract the signal independent on magnetic field, the optical response of the normalized Kerr signal as a function of delay between pump and probe pulse is proportional to the out-of-plane magnetization dynamics. For more details on the pump-probe setup and measurement procedure, see Appendix A.

C. Constant and pulsed field initialization of the magnetic state

The stroboscopic nature of pump-probe experiments requires the initialization of the magnetic state after each excitation-detection cycle. This can be achieved by applying a constant magnetic field, which, however, not only reinitializes the sample, but also affects the magnetization dynamics in the entire time window following the excitation. In order to circumvent this drawback of the constant field initialization, we reset the sample magnetization in the second configuration by applying comparably short out-of-plane *magnetic field pulses* of 40 μs duration. The pulses have an amplitude of approximately 60 kA/m and are generated by a low-inductance coil brought very close to the sample. The coil has a significantly larger diameter than the extent of the probe laser spot and thus generates there a comparably homogeneous magnetic field as in the constant field measurements. The timing scheme showing the pump, probe, and magnetic reset pulses is sketched in Fig. 1. The magnetic field pulses are synchronized with the laser repetition rate of 1 kHz, but shifted by 0.5 ms into the middle of the time interval between two successive pump-probe cycles. We note that, by magnetic pulsing, we were able to gain direct access to the *intrinsic* magnetization relaxation, i.e., the relaxation dynamics unaffected by the external magnetic field.
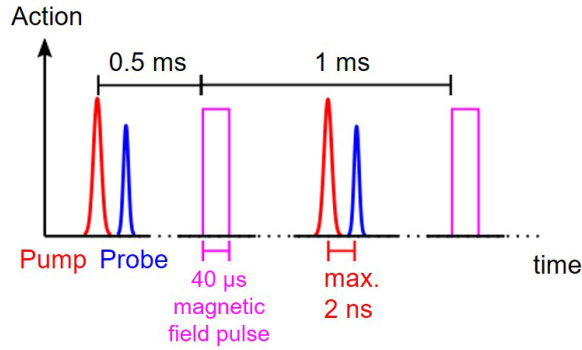
FIG. 1. Timing scheme for the pump-probe measurements with magnetic state initialization by magnetic field pulses, which are synchronized with the laser repetition rate and applied in the middle of the time interval between two successive optical pump pulses.

D. Measurement of transient hysteresis loops

In order to record snapshots of the evolution of the hysteretic magnetization behavior at a fixed delay time t_d, we recorded series of so-called *transient hysteresis loops*. These were measured by fixing the pump-probe delay time and recording the change of the TR-P-MOKE signal as a function of applied external magnetic field in the range of $H = \pm 80 \, \text{kA/m}$, similar to the procedure described in [46].

III. 3TM-BASED AND PHENOMENOLOGICAL RESPONSE FUNCTIONS

Experimental transient magnetization curves are analyzed by fitting response functions to extract relevant parameters. We distinguish (i) response functions that are solutions to one of the various versions of the 3TM and (ii) purely phenomenological response functions. The latter are commonly used in the literature [29,30,47–54] to extract empirical time constants and potentially guide theoretical model development.

A. 3TM-based response functions

In the standard 3TM, the dynamics of the electron, spin, and lattice systems are described in terms of thermal energy flow between separate but interacting reservoirs, which are assigned different effective temperatures T_e, T_s, and T_l, respectively [2]. The system of differential equations describing the dynamics of the 3TM system is in general not solvable analytically without simplifying assumptions. In the perturbative regime (low pump laser fluence), where the heat capacity of the spin system can be neglected, the spin and electron temperatures evolve in the same way ($T_s = T_e$) and the 3TM reduces to the 2TM. An analytical solution of the 2TM was given by van Kampen *et al.* [26] and later improved by Dalla Longa *et al.* [55]. However, our experiments were performed well outside the limits of the perturbative regime, as we used large pump laser fluences that led to magnetization quenching of up to 100%. The high fluence regime is described by the M3TM [27] that allows the spin temperature to reach T_C, i.e., full magnetization quenching. Both the 3TM and M3TM have a validity limit below 100 ps and are not suited to describe our target timescale of up to nanoseconds. Recently, a model

has been developed that extends the validity to a broader time interval, namely the extended microscopic three-temperature model (eM3TM) [45], which additionally accounts for the heat flow from the lattice system to the thermal reservoir of the substrate kept at constant temperature T_a. Such thermal diffusion of energy via the lattice is also included in the extended three-temperature model (E3TM) [44], although it was developed primarily to account for the excitation of nonthermal electrons during the first picoseconds and the subsequent energy flow from the nonthermal electrons to the thermal electron, lattice, and spin subsystems (for a full description of both extended models, see Appendix F). In both models [44,45], the inclusion of the heat flow to the substrate describes the dissipation of the energy input of the pump laser pulse into the substrate, which enables the system to completely relax to the initial state (magnetization and temperature) before laser excitation. In the eM3TM, the differential equation describing the evolution of lattice temperature [see Eq. (F1b) in Appendix F] is extended by a second term,

$$\left(\frac{dT_l}{dt}\right)_{\text{Substr.}} = \frac{(T_a - T_l)}{\tau_a},$$

where τ_a is the characteristic time constant of the heat flow from the sample to the substrate. In the E3TM, the heat flow to the substrate is modeled in terms of thermal diffusion characterized by the coefficient K_l [see Eq. (F2c) in Appendix F] described as

$$\left(C_l \frac{dT_l}{dt}\right)_{\text{Substr.}} = -K_l(T_l - T_a)^3,$$

where C_l is the heat capacity of the lattice system. The response functions for the normalized transient magnetization $m(t) = M(t)/M_s$ of both models cannot be determined analytically, but can be obtained for a given set of parameters by numerical integration of the differential equations. We applied both the E3TM and the eM3TM to fit our data. We note, however, that neither of the two models is able to describe our measured data in the full time interval. For details and the fitting curves, see Appendix F. Key results are shown in Figs. 3(d), 3(e), 5(e), and 5(f) and discussed in Sec. VII.

So far, no magnetic field dependence of the magnetization relaxation on long timescale has been considered in any 3TM based models. The effect of the external magnetic field can be included in the M3TM because it contributes to the effective field in the material as does the field due to the inverse Faraday effect [42]. However, the validity of the M3TM is limited to short timescales (<100 ps). Therefore, no existing model accounts for the effect of the external magnetic field on longer timescales up to nanoseconds.

B. Phenomenological response function

In order to fit ultrafast magnetization relaxation measurements and to extract characteristic time constants, several authors [30,48,51] applied a phenomenological response function that has been inspired by the analytical solution of the 2TM. For this approach, the simplified expression for the evolution of the electronic temperature $\Delta T_e(t)$, which contains only the zero-order harmonics of the full expression [56], is

considered,

$$\Delta T_e(t) = \Delta T_1 (1 - e^{-(t-t_0)/\tau_m}) e^{-(t-t_0)/\tau_E}$$
$$+ \Delta T_2 (1 - e^{-(t-t_0)/\tau_E}). \quad (1)$$

ΔT_1 is the temperature increase of the electron system in the absence of electron-phonon relaxation and ΔT_2 is the temperature increase of the electron system after the electron-phonon relaxation. The two time constants τ_m and τ_E represent the characteristic timescales of the energy transfer from the photons to the electron reservoir (τ_m: ultrafast demagnetization) and the subsequent energy flow from the electron to lattice reservoir (τ_E: electron-phonon relaxation). In general, changes of the normalized transient magnetization are, to the first approximation, proportional to changes of the spin temperature, $\Delta m(t) \propto -\Delta T_s(t)$ [57]. Considering this, the spin temperature can be substituted by the electron temperature $\Delta m(t) \propto -\Delta T_e(t)$, therefore rendering Eq. (1) a phenomenological response function. The phenomenological response function constructed in this way has been widely employed to extract empirical demagnetization and relaxation times τ_m and τ_E, respectively. However, the majority of the published results on transients is limited to subnanosecond timescales [29,30,47,48,51] for the magnetization dynamics data.

We attempted to fit our experimental data with Eq. (1) and could find matching fits only in the time window below 100 ps. At timescales *exceeding* 100 ps, all fitting attempts showed substantial deviations between fitted and measured curves (see Fig. 10 of Appendix E). In order to extract phenomenological time constants at all timescales, including the nanosecond time range, we modified Eq. (1) by multiplying the second term with an additional exponential factor $e^{-(t-t_0)/\tau_s^*}$. The resulting modified phenomenological response function then reads

$$m(t) = G(t) \otimes \{1 - \Theta(t - t_0)[A_1(1 - e^{-(t-t_0)/\tau_m^*}) e^{-(t-t_0)/\tau_f^*}$$
$$+ A_2(1 - e^{-(t-t_0)/\tau_f^*}) e^{-(t-t_0)/\tau_s^*}]\}. \quad (2)$$

Here, $G(t)$ is a Gaussian function with a full width at half maximum (FWHM) of 80 fs, which represents the temporal intensity profile of the femtosecond probe pulse and is convoluted with the main body of the response function, and $\Theta(t - t_0)$ is the Heaviside step function. Since our modification is purely phenomenological, we also replace τ_m and τ_E by *phenomenological* time constants τ_m^* and τ_f^*. τ_m^* is the phenomenological time constant of magnetization quenching, τ_f^* and τ_s^* are phenomenological time constants describing fast (ps) and slow (ns) magnetization relaxation processes, respectively. In particular, the additional exponential factor $e^{-(t-t_0)/\tau_s^*}$ containing the characteristic time τ_s^* is intended to describe relaxation slowdown on the nanosecond timescale. A_1 represents the normalized amplitude of the magnetization quenching that would be achieved in the absence of any relaxation. A_2 is a measure of the strength of the relaxation slowdown. It indicates the remaining magnetization quenching level at the time when, in the absence of relaxation slowdown ($A_2 = 0$), the subsystem temperatures would reach equilibrium and the normalized transient magnetization would return to saturation, $m(t) \approx 1$ (see Appendix C). We note that fitting with Eq. (2) results, compared to Eq. (1) and the above-
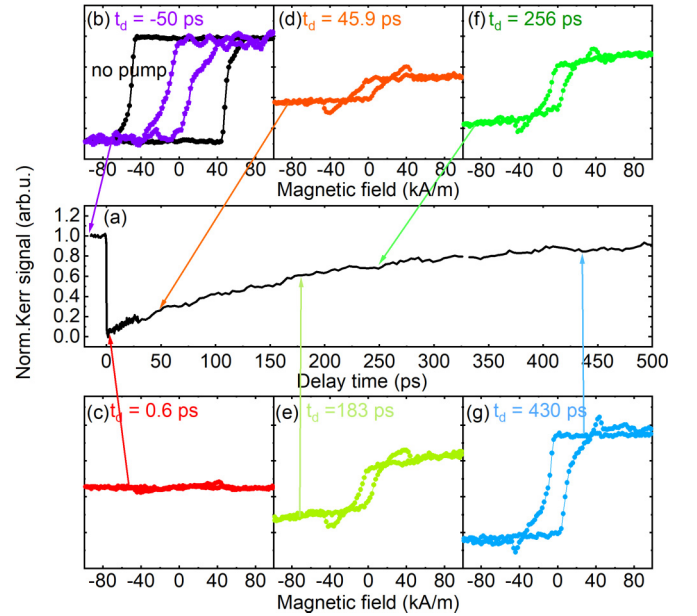
FIG. 2. The demagnetization curve in (a) shows the evolution of the magnetization of the $[Co/Pt]_3$ multilayer after excitation with an optical pulse with fluence of $18 \, mJ/cm^2$ measured in a static field of 80 kA/m. (b)–(g) Transient hysteresis curves measured at different fixed probe time-delays t_d, as marked with colored arrows. The purple curve in (b) shows the hysteresis 50 ps before the excitation pulse, i.e., approximately 1 ms after the preceding pump pulse, whereas the black curve represents the static hysteresis measured without applying pump pulses.

mentioned models, in a substantial improvement of the fits for timescales exceeding 100 ps, while keeping the fits at shorter timescales intact (see Fig. 10 of Appendix E). The possible meaning of τ_s^* in terms of physical processes associated with magnetization relaxation is discussed below.

We emphasize again that our modified response function is referring neither to the pure electronic temperature evolution nor to the solution of any version of the 3TM. Equation (2) is a *phenomenological equation* that yields unique global fits of magnetization transients with a minimum number of free parameters and can be used to extract phenomenological magnetization relaxation time constants.

IV. TRANSIENT MAGNETIZATION HYSTERESES *M* VS *H*: FIELD DEPENDENT SNAPSHOTS OF MAGNETIZATION RELAXATION

Figure 2 displays the optically induced TR-P-MOKE dynamic signal of a $[Co/Pt]_3$ multilayer. In the data displayed in the main Fig. 2(a), a magnetic field of 80 kA/m is applied perpendicular to the surface and is kept constant during the entire transient measurement. We applied a pump laser fluence of $18 \, mJ/cm^2$ that induces the largest achievable magnetization quenching without a permanent structural modification of the sample (for details on determining the pump laser fluence threshold for sample modification, see Appendix B). After recording the transient magnetization curve, we measured a series of transient hysteresis loops following the procedures described in Sec. II D; see Figs. 2(b)–2(g). We note that the

transient magnetization values $m_S(t_d)$ obtained after reaching magnetization saturation in these transient hysteresis loops match the $m(t_d)$ values in the dynamic measurement taken in a static and saturating field $H = 80\,\text{kA/m}$, as illustrated by the colored arrows in Fig. 2(a).

The black curve marked in Fig. 2(b) as "no pump" shows the normalized P-MOKE signal in the absence of pump pulses. This static loop displays high squareness with a coercive field $H_c = 50\,\text{kA/m}$, which indicates a strong perpendicular magnetic anisotropy (PMA) [58]. For the later analysis below, the absolute difference between two magneto-optic signal levels for $H = \pm 80\,\text{kA/m}$, extracted from static hysteresis, was used as *initial magnetic contrast* for normalization. Figure 2(c) shows that the hysteresis loop nearly completely collapses [$m_S(t_d) \approx 0$] at the time of maximum quenching, $t_d = 0.6\,\text{ps}$ after the excitation. After reaching this full demagnetization, $m_S(t_d)$ continuously returns to its dynamic equilibrium after about 500 ps after the excitation. Figures 2(d)–2(g) illustrate transient hysteresis loops measured at different fixed delay times t_d. We stress that although the transient hystereses show clear $m_S(t_d)$ recovery, the transient coercive field $H_c'(t_d)$ remains suppressed by almost 50%, even at delay times more than *one millisecond* after the optical excitation. This long-delay transient hysteresis was obtained by adjusting the delay line at the position just before the zero delay [e.g., $t_d = -50\,\text{ps}$ in Fig. 2(b)], thus allowing the sample 1 ms recovery time.

In order to trace even longer relaxation, we decreased the laser repetition rate from 1 kHz to 200 Hz to achieve time intervals up to 5 ms between successive pump-probe cycles. As a result, the transient hysteresis loops recover gradually and reach almost the shape of the static one at 3 ms pulse interval (see Fig. 9 in Appendix D). Our observations clearly reveal that the recovery of the transient coercive field $H_c'(t_d)$ takes much *longer* than that of the transient saturation magnetization $m_S(t_d)$. This fact as well as a significant change of the shape of the transient hysteresis indicates that the sample has still not relaxed into its thermodynamic equilibrium even 5 milliseconds after the pump pulse. This observation may be important in the context of toggle switching.

V. IMPACT OF THE EXTERNAL FIELD

In this section, we present results on the influence of the external magnetic field on fs laser-induced magnetization dynamics of $[\text{Co/Pt}]_3$ multilayers. We recorded the transients in a relatively broad time window ranging from a few femtoseconds up to two nanoseconds after the laser excitation and focused our examination on the processes that drive the magnetic system back to equilibrium. The field dependent magnetization dynamics $m(H_i, t)$ were measured at six different static magnetic fields intensities H_i ($i = 1 \ldots 6$), ranging from $H_1 = 11\,\text{kA/m}$ to $H_6 = 91\,\text{kA/m}$ [see Fig. 3(a)]. The fluence of the pump laser pulse was kept constant at $18\,\text{mJ/cm}^2$. All the transient curves are normalized to the *initial magnetic contrast* as defined in Sec. IV.

Figure 3(a) shows the demagnetization curves near zero delay in the time window from -2 to 1 ps in linear-linear axis scale. The rest of the time window is shown in a logarithmic timescale. The measurements show that the transient curves
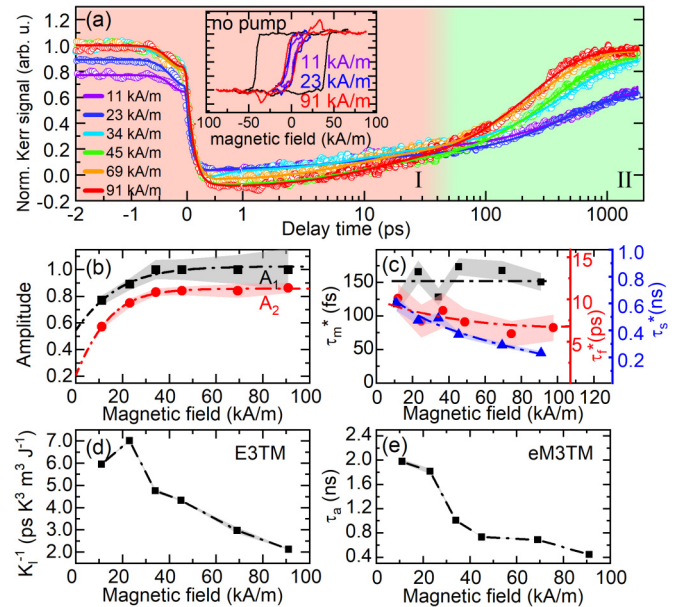
FIG. 3. TR-P-MOKE measurements on $[\text{Co/Pt}]_3$ for different applied magnetic fields. (a) Evolution of the magnetization after the optical excitation in the time range -2 to 2000 ps. The data is plotted on a linear timescale from -2 to 1 ps and on a logarithmic timescale from 1 to 2000 ps. Differently colored symbols represent the data for different field strengths as indicated. The solid lines represent the corresponding fits with Eq. (2). Insets in (a) show minor hysteresis curves with different field sweep maxima H_i as indicated and taken at $t = -50\,\text{ps}$, i.e., just before the pump pulse, approximately 1 ms after the previous excitation. Red and green background colors indicate regions I and II, where the relaxation is weakly and strongly affected by the magnetic field, respectively. Panel (b) shows the fit amplitudes A_1 and A_2 as a function of applied magnetic field and (c) the extracted time constants τ_m^* (black squares), τ_f^* (red circles), and τ_s^* (blue triangles). Panel (d) shows the inverse thermal diffusion coefficient K_l^{-1} extracted from fits with the E3TM as a function of applied magnetic field and (e) the time constant τ_a extracted from fits with the eM3TM. Dash-dotted lines in (b)–(e) are guides to the eye and the shaded areas in (b) and (c) connect the error bars of the corresponding data points.

nearly overlap during the initial approximately 60 ps. The transients measured in applied fields below 34 kA/m start with a lower value before time zero. This reduced normalized magnetization value is attributed to an incomplete recovery of the minor hysteresis loop. This is illustrated by the insets in Fig. 3(a), where we show minor hysteresis curves for $t = -50\,\text{ps}$ with different field sweep maxima corresponding to selected H_i values. The $m(t)$ curves start to deviate significantly from each other for delay times exceeding 40 ps. At this point, the relaxation process can be divided into two separate time regions I and II, marked as red and green areas in Fig. 3(a). Obviously, the transient magnetization $m(H_i, t)$ in region I is almost unaffected by the external field compared to region II. The behavior in region I is similar to that reported in [28] also for $[\text{Co/Pd}]_N$, where the authors demonstrated the independence of the relaxation rate on magnetic field within the first 10 ps. In region II, stronger applied magnetic fields tend to speed up the magnetization relaxation. Our results

show that the effect of the external field affects the transient curves significantly only for times exceeding 40 ps.

The $m(H_i, t)$ curves were fitted using the phenomenological response function in Eq. (2) as well as with the response functions obtained from the eM3TM and the E3TM by numerical integration of the sets of differential equations [see Eqs. (F1a)–(F1d) and (F2a)–(F2e) in Appendix F]. The best fits were obtained with Eq. (2) and are included in Fig. 3(a) as solid lines. All parameters extracted from fitting $m(t)$ curves with Eq. (2) are compiled in Table I of Appendix E. The fitting curves for the eM3TM and E3TM are shown in Figs. 11 and 12 of Appendix F.

Figure 3(b) shows the extracted amplitudes A_1 and A_2 of Eq. (2) as function of the external magnetic field. Both A_1 and A_2 increase monotonically with the increasing external field, and A_1 exceeds A_2 by 10–20% in the entire magnetic field range. Figure 3(c) shows that $\tau_s^*(H)$ drops strongly from 0.6 to 0.2 ns when the applied magnetic field increases from 11 and 91 kA/m, whereas $\tau_f^*(H)$ shows a weaker decrease from 10 to 7 ps and τ_m^* is approximately independent of H. When fitting the data with the eM3TM and the E3TM, the magnetic field dependent magnetization relaxation on long timescales yields magnetic field dependencies of the thermal diffusion coefficient K_l of the E3TM and the time constant τ_a of the eM3TM, as shown in Figs. 3(d) and 3(e), respectively. Both $K_l^{-1}(H)$ and $\tau_a(H)$ follow the same trend as $\tau_s^*(H)$ and also decrease in the measured magnetic field interval by a factor of 3–5. However, a magnetic field dependence of K_l and τ_a completely contradicts the assumptions of the eM3TM and the E3TM, where these parameters describe the heat flow from the lattice system to the thermal reservoir of the substrate, which is at the constant temperature T_a. If we force K_l and τ_a to be *constants* in the fitting procedure (as required by the assumptions of the eM3TM and the E3TM), the fitting strongly deteriorates and fails to reproduce the experimental data on timescales exceeding 200 ps.

VI. IMPACT OF LASER FLUENCE

In order to investigate the magnetic field dependent relaxation process on the long timescale in more detail, we measured the magnetization dynamics as a function of laser fluence. These measurements were carried out with constant and pulsed field initialization of the magnetic state; see Fig. 1 in Sec. II C. In the first configuration [Fig. 4(a)], an external magnetic field of 80 kA/m was applied *continuously* and perpendicular to the sample surface. The laser fluence was varied from 3 to 19.1 mJ/cm². In the second configuration [Fig. 4(b)], we reset the sample magnetization by applying comparably short *magnetic field pulses* of 40 μs duration between successive pump-probe cycles.

In both Figs. 4(a) and 4(b), we observe for pump fluence up to 15 mJ/cm² that the quenching amplitude remains the same, regardless of whether the magnetization is reset by a continuous or pulsed magnetic field. It is remarkable, however, that the transient behavior beyond 10 ps is very different for magnetic field-influenced relaxation (constant field) and intrinsic relaxation (pulsed field). Contrary to a Fig. 3, the delay time at which the curves start to deviate from each other strongly varies with increasing fluence. In Fig. 4(a), this
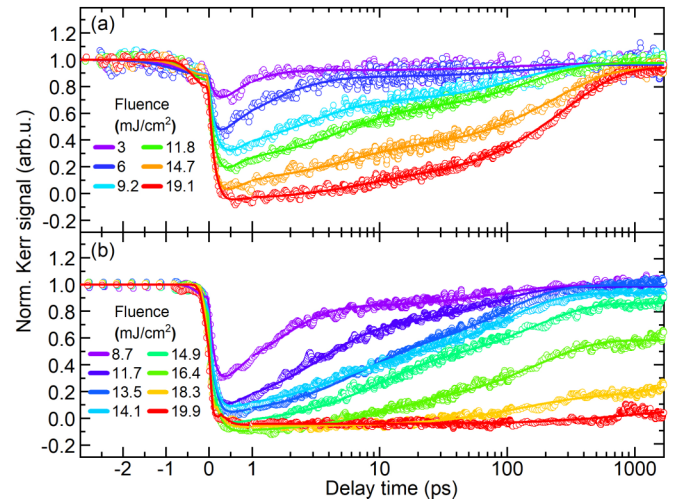
FIG. 4. TR-P-MOKE measurements on [Co/Pt]₃ for different laser fluence with (a) constant magnetic field of 80 kA/m and (b) pulsed magnetic field. The data are plotted from −2 to 1 ps using a linear timescale and from 1 to 2000 ps using a logarithmic timescale. Differently colored symbols represent the data taken at different laser fluence as indicated. Solid lines represent the corresponding fits with Eq. (2).

leads to a relaxation slowdown that shifts the time of reaching magnetization saturation from about 2 ps at low fluence (3 mJ/cm²) to almost 1 ns for highest fluence (19.1 mJ/cm²). With increasing fluence, the shapes of the $m(t)$ curves cannot be described by the double-exponential form of Eq. (1), but can be fitted very well by Eq. (2). The impact of the laser fluence is even stronger in Fig. 4(b), where $m(t)$ recovers to its initial state only at low pump fluence within the observation time window. If the pump fluence exceeds 19 mJ/cm², the demagnetized state $[m(t) \approx 0]$ persists up to 2 ns.

As in Sec. V, we analyze the data by fitting them with the phenomenological response function in Eq. (2) as well as with the response functions of the eM3TM and the E3TM. The best fits were again obtained with Eq. (2) and are superimposed in Fig. 4 as solid lines. For a compilation of all parameters extracted from fitting $m(t)$ curves with Eq. (2), see Tables II and III of Appendix E. The fitting curves for the eM3TM and the E3TM are shown in Figs. 11–13 of Appendix F.

Figures 5(a)–5(d) show the fluence dependencies of the amplitudes A_1 and A_2 as well as the time constants τ_m^*, τ_f^*, and τ_s^*, extracted by fitting the transient curves in Fig. 4 with Eq. (2). Black and red symbols represent the constant and pulsed magnetic field configuration, respectively. From Fig. 5(a) we see that both amplitudes A_1 (full squares) and A_2 (open circles) increase with increasing pump fluence and are independent of the presence of an external magnetic field. A_1 is linearly proportional to the laser fluence in the range from 3 to 15 mJ/cm² and then approaches saturation for higher laser fluence, while A_2 shows an increasing trend with an opposite curvature. The time constants τ_m^*, τ_f^*, and τ_s^* as functions of pump fluence are shown in Figs. 5(b)–5(d), respectively. The demagnetization time τ_m^* stays constant ($\tau_m^* \sim 160$ fs) within error intervals over most of the laser fluence range and shows
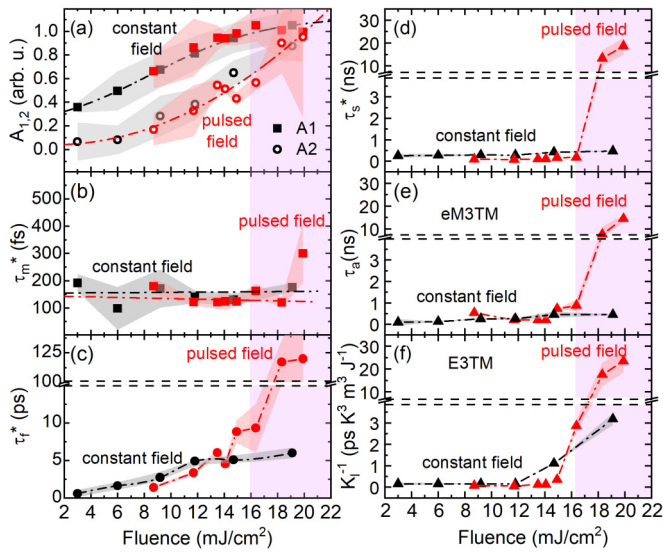
FIG. 5. (a)–(d) Fit parameters obtained by fitting the data in Fig. 4 with the phenomenological response function [Eq. (2)] as a function of laser fluence. (a) Amplitudes A_1 (solid squares) and A_2 (open circles), (b) τ_m^*, (c) τ_f^*, and (d) τ_s^*. Panel (e) shows the time constant τ_a extracted from fits with the eM3TM and (f) the inverse thermal diffusion coefficient K_l^{-1} extracted from fits with the E3TM as a function of laser fluence. Black and red symbols represent the constant and pulsed magnetic field configuration, respectively. Dash-dotted lines in are guides to the eye and the shaded areas in connect the error bars of the corresponding data points. Note the split ordinates in (c)–(f).

only a single point increase at the largest applied laser fluence value in the pulsed field configuration.

In contrast, the relaxation time τ_f^* increases steadily with increasing laser fluence in both the constant and pulsed field configurations. For the constant field case, the τ_f^* values scale linearly with laser fluence in the entire range from 3 to 19.1 mJ/cm². A significant difference between the constant and pulsed field configurations appears around 16 mJ/cm², where for the latter case τ_f^* increases abruptly from 9 to 120 ps between 16 and 19.1 mJ/cm². This steep, 13-fold increase coincides with the region of fluences, where A_1 approaches 1.0, i.e., complete demagnetization. A very similar effect can also be observed for τ_s^* in Fig. 5(d). At a relatively low fluence from 3 to 16 mJ/cm², the τ_s^* values weakly vary for both magnetic field configurations between 0.1 and 0.3 ns. For laser fluences exceeding ~16 mJ/cm², τ_s^* increases in the pulsed field configuration abruptly by more than 60 times and reaches nearly 20 ns at 19.1 mJ/cm². We emphasize that the abrupt increases in relaxation times τ_f^* and τ_s^* are solely present for the pulsed magnetic field configuration, where the magnetization relaxation is not affected by the external magnetic field.

Figures 5(e) and 5(f) show the fluence dependence of the parameters τ_a and K_l^{-1} obtained by fitting the data in Fig. 4 with the eM3TM and the E3TM, respectively, where they can vary with pump laser fluence. The results for τ_a are almost identical to those for τ_s^* for both constant and pulsed field measurements. The results for the E3TM in Fig. 5(f) show a significant apparent decrease of the thermal diffusion constant K_l when the fluence exceeds 12 mJ/cm². Similar to Sec. V,

the parameters τ_a and K_l^{-1} follow qualitatively the behavior of τ_s^*, but now as a function of pump laser fluence. However, as for the field dependence discussed above, the fluence dependence of τ_a and K_l is also in conflict with the assumptions of the eM3TM and the E3TM that these parameters describe the heat flow from the lattice system to the thermal reservoir of the substrate. If the parameters τ_a and K_l are kept constant, the fitting of the experimental data with the E3TM and the eM3TM strongly deteriorates and fails to reproduce the experimental data on timescales exceeding 200 ps.

VII. DISCUSSION AND QUALITATIVE DYNAMIC MODEL

Our measurements of relaxation processes in [Co/Pt]₃ multilayers in the time interval up to 2 ns after laser excitation revealed significant deviations from the relaxation dynamics described by the existing extended three-temperature models (E3TM, eM3TM). Pronounced deviations of the measured $m(t)$ time traces from those calculated with the extended models suggest the presence of a relaxation slowdown mechanism on the timescale beyond 100 ps, which depends on both pump laser fluence and applied magnetic field. Laser fluence dependent measurements reveal that both here-introduced phenomenological time constants for fast τ_f^* and slow τ_s^* magnetization relaxation show an enormous enhancement (magnetization relaxation slowdown), if (i) the multilayers reach their demagnetization limit (full quenching corresponding to $A_1 \approx 1$) and (ii) the relaxation is intrinsic in the sense that it is not driven by an external magnetic field. Both (i) and (ii) must be satisfied to observe this extremely large relaxation slowdown. In addition, we demonstrate that the multilayers do not entirely reach their magnetic equilibrium state even several *milliseconds* after the optical excitation, which manifests itself in an extremely long relaxation time of the transient coercive field $H_c'(t_d)$ in the *millisecond* range.

Both tested extended three-temperature models (E3TM, eM3TM) were unable to describe the relaxation slowdown on timescales exceeding 200 ps. We obtained the best fitting results using a phenomenological response function [Eq. (2)], which we constructed by including the term $e^{-(t-t_0)/\tau_s^*}$ into a phenomenological response function reported earlier. We interpret the magnetization relaxation behavior in the framework of the concepts developed in the Landau-Lifshitz-Bloch model and with numerical solutions [Fig. 6(a)] of the E3TM, which fits our data very well for timescales <200 ps (see Appendix F 2). The development of a self-consistent theory is beyond the scope of the present study, but by following our assumptions, we present in Fig. 6 an intuitive physical picture of the relaxation processes.

After the pump laser pulse has induced an ultrafast demagnetization process on the timescale of τ_m, we consider two main relaxation mechanisms driving the demagnetized area back to the equilibrium. First, the so-called longitudinal relaxation mechanism re-establishes the magnetization amplitude. This happens on the picosecond timescale and is associated with the cooling of the spin temperature T_s, as shown in Fig. 6(a) and phenomenologically described by the relaxation time τ_f^*. Second, transverse damping describing LLB-type damping of precessional motion gives rise to relaxation on timescales exceeding 100 ps. We note that the latter process is
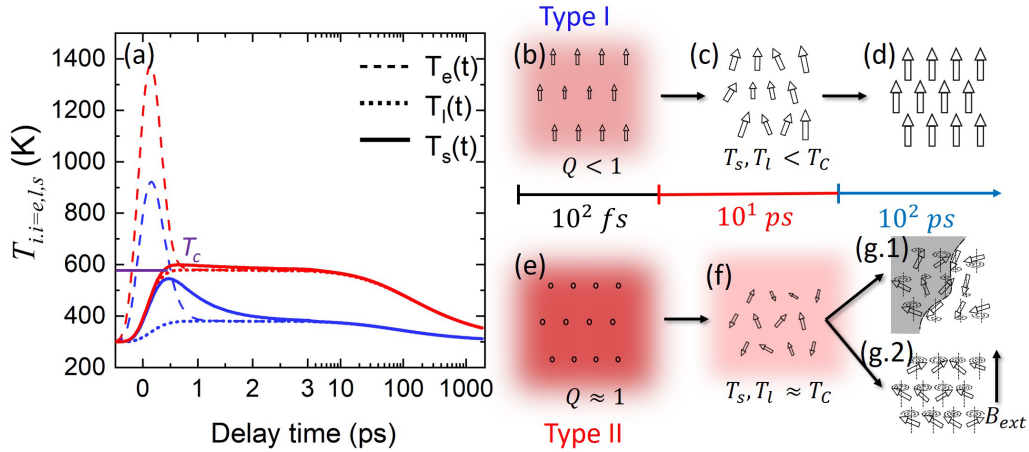
FIG. 6. Qualitative model for laser-induced magnetization relaxation at low (type I) and high (type II) laser fluence. (a) Numerical solutions of the E3TM for the evolution of the electron (dashed), lattice (dotted), and spin (solid) temperatures at low (6 mJ/cm², blue) and high (19.1 mJ/cm², red) fluence on a split linear (−0.5 to 3 ps) and logarithmic (3 ps to 2 ns) time axis. The purple horizontal line indicates the Curie temperature T_C of the Co/Pt multilayers. The arrows in (b)–(g) schematically illustrate the magnetization vector field and its spatial fluctuations in magnitude and direction for the two cases at selected time delays after the laser pulse excitation. (b),(e) The quenching Q of the magnetization magnitude depends on the laser fluence and strongly differs for the two cases. (c),(f) The magnetization magnitude recovers by longitudinal damping within several picoseconds to more than 100 ps depending on the degree of quenching Q and the evolution of the spin temperature. (d),(g) The transverse damping of precessional motion occurs on a longer timescale and becomes dominant after the longitudinal relaxation. Panels (g1) and (g2) schematically depict the behavior without and with applied magnetic field, respectively.

tunable by the applied magnetic field. Here, we propose that the transverse damping, contributing to the long relaxation times, is characterized by the time constant τ_s^*, which we introduced into the phenomenological $m(t)$ response function via the term $e^{-(t-t_0)/\tau_s^*}$ [Eq. (2)].

According to the E3TM a pump pulse at time zero subsequently leads to a transient increase of three different temperatures of the spin (T_s), electron (T_e), and phonon (T_l) reservoirs. The evolution of the temperatures is shown in Fig. 6(a) based on numerical solutions of the E3TM. Blue and red curves correspond to the low and high fluence cases (types I and II). The two calculations were performed using the best fitting parameters for the magnetization transients measured for pump laser fluence 6 and 19.1 mJ/cm², respectively, and with constant field magnetic state initialization [Fig. 4(a)]. All calculation parameters are listed in the Table IV in Appendix G. Energy transfer from the laser pulse to the electrons raises the nonthermal electron energy density N [see Eqs. (F2) in Appendix F] almost instantaneously (<100 fs). After a time delay of the order of τ_M, heat transfer to the spin reservoir increases T_s, resulting in a reduction of the magnetization amplitude, i.e., a longitudinal quenching of magnetization as shown in Figs. 6(b) and 6(e). For low pump laser fluence, T_s and T_e cool down on the timescale of a few picoseconds (characterized in the perturbative regime by $\tau_E = C_e/g_{el}$) giving rise to fast magnetization relaxation within picoseconds (type I relaxation). However, for high pump laser fluence, the nonthermal electron energy density is much higher and the energy flow from nonthermal electrons to the thermal electron and spin reservoirs remains significant for a much longer time and competes with the heat drain to the lattice. As a result, the magnetization relaxation is slowed down to timescales of 100 ps to nanoseconds (type II relaxation). This type-I to type-II transition has been de-

scribed by Shim *et al.* [44]. In our phenomenological response function, it leads to a fluence dependent but magnetic field independent increase of the phenomenological time constant τ_f^*. The temperature of the lattice system T_l responds slower to the laser excitation. After tens of picoseconds the three reservoirs reach the thermal equilibrium at a slightly higher temperature than the environment T_a. Heat flow from the multilayer to the substrate described in the E3TM by the K_l term [Eq. (F2c) in Appendix F] and in the eM3TM by the τ_a term [Eq. (F1b) in Appendix F] eventually allows the multilayer to relax within nanoseconds to its initial temperature and magnetization before the laser excitation. This slow relaxation is phenomenologically included in the τ_s^* term of our response function [Eq. (2)] as is evident from $m(\infty) = m(0) = 1$, which also describes the complete relaxation to the initial state. As an *additional* relaxation channel, we expect that the heat flow to the environment contributes as a small *negative* and magnetic field independent contribution to A_2, i.e., it reduces the strength of the relaxation slowdown.

At the moment we are not aware of physical mechanisms leading to magnetic field dependent thermal heat diffusion. Therefore, the observed dependence of the relaxation behavior on the external magnetic field, reflected in the field dependencies of τ_f^* and τ_s^* [Figs. 3(c), 5(c), and 5(d)], cannot be explained in the framework of the mechanisms discussed above. Possible mechanisms are qualitatively discussed below.

Our phenomenological model distinguishes two types of relaxation for low and high pump laser fluence, respectively.

Type I [Figs. 6(b)–6(d)] applies when the spin temperature after the laser-induced increase is small compared to T_C of the sample, as indicated by the blue solid curves in Fig. 6(a). In this case, the degree of magnetization quenching Q is relatively low, so that a significant residual magnetization and magnetic anisotropy remain and act as a "memory" of

the initial magnetic state. A few picoseconds after laser excitation, the three temperatures T_e, T_s, and T_l converge due to energy exchange among the reservoirs and the LLB-type longitudinal magnetization relaxation is complete. However, the local temperature is elevated compared to the environment and causes fluctuations of the magnetization direction [Fig. 6(c)]. Accordingly, the remaining magnetization dynamics is dominated by precessional motion of local moments, which relax via LLB-type transverse damping on the nanosecond timescale and, thus, slow down the relaxation. Since the precessional damping is field dependent, this relaxation slowdown results in a magnetic field dependence of the phenomenological time constant τ_s^*. Such precessional motion includes for instance heat-driven domain wall motion [59,60] and magnon generation [41,61]. Finally, the thermodynamic equilibrium with the environment and magnetization saturation are reached within nanoseconds [Fig. 6(d)].

Type II [Figs. 6(e)–6(g)] applies for a high laser fluence that results in a complete magnetization quenching *Q,* meaning that the memory of the initial magnetic state is lost. As a consequence, not only the longitudinal relaxation takes longer time. The higher temperature ($T_e \approx T_s \approx T_l$) close to T_C, which cools much slower, also delays the relaxation, and results in much stronger fluctuations of the magnetization direction [Fig. 6(f)], reflecting the lost memory. These consequences of the lost memory cause the sharp increase of τ_f^* for $Q \approx 1$ [pulsed field case in Fig. 5(c)]. The longitudinal relaxation is accompanied by the re-establishment of spin-orbit coupling and exchange interaction in the system [2]. The re-emerging magnetocrystalline anisotropy and the external magnetic field act as an effective anisotropy, which becomes the major driving force of domain formation counteracting thermal fluctuations on the microscopic lateral length scale.

If no external field is applied [Fig. 6(g1)], after the longitudinal recovery, a random distribution of domains develops in time, since both directions of an uniaxial anisotropy contribution (e.g., up and down) are energetically equivalent in the field-free case. The magneto-optic probing, averaging over the signal from a large ensemble of micrometer-sized domains, measures a zero net magneto-optic signal. The formation of large domains, from which an approximately single-domain (ground) state can develop and resulting in a nonzero magneto-optic signal, occurs on timescales beyond 2 ns [e.g., red curve Fig. 4(b)]. This delayed domain formation causes the sharp increase of τ_s^* by more than one order of magnitude for laser fluences above the threshold, where $Q \approx 1$ is reached [pulsed field case in Fig. 5(d)]. If the external field is applied [Fig. 6(g2)], it tends to align the magnetization direction as soon as the longitudinal magnetization recovery sets in, explaining the absence of the abrupt increase of τ_s^* for $Q \approx 1$ [constant field case in Fig. 5(d)]. By increasing the external field, the effective anisotropy becomes stronger and more unidirectional, so that large domains can form faster. Such a field dependence of the recovery rate is reflected in the field dependence of τ_s^* [Fig. 3(c)].

We note that for 3d transition-metal ferromagnets and in particular Co/Pt multilayers, precessional motion does not play a significant role during the first 10 ps after excitation, since such fast damping would be orders of magnitude faster than reported in, e.g., [36], or observed in ferromagnetic res-

onance measurements [62]. The timescale is far too short for the magnetization vector to pass through even a fraction of a precession cycle.

Finally, we address the relaxation on the millisecond timescale seen in transient hysteresis loops. The observed recovery of $m_S(t_d)$ suggests that the sample has substantially cooled down after several nanoseconds and the multilayer has reached a temperature far below T_C. However, the shape of the hysteresis loops and the coercive fields $H_c'(t_d)$ still deviate from the static behavior even several milliseconds after the laser excitation (Fig. 9 of Appendix D). This observation points towards a nonequilibrium domain structure with a low number of small residual domains or small areas with noncollinear magnetization. Such structures are metastable and may result from rapid cooling within nanoseconds and spatially inhomogeneous magnetization, anisotropy, and temperature distributions. These small deviations from the ideal ferromagnetic ground state may reduce the macroscopic magnetization by only a few percent, i.e., below the detection limit of the transient hysteresis loop measurements. On the other hand, their high susceptibility to an applied magnetic field can significantly influence the hysteresis shape and reduce the coercive field considerably. Residual domains, for instance, are stabilized by magnetic anisotropy or pinning, but can be removed from the sample with a weak opposing magnetic field via domain wall motion.

VIII. CONCLUSIONS

We studied magnetization dynamics in [Co/Pt]$_3$ multilayers after optical excitation by linearly polarized pump laser pulses of 80 fs FWHM and 1 kHz repetition rate. Tuning the pump laser fluence allowed to either partially or completely demagnetize the sample on the timescale of 100 fs. The recovery of the magnetization after this controlled quenching was monitored magneto-optically during 2 ns. Measurements over such a comparably long time window are, to our knowledge, quite rare, but of utmost importance for understanding the optically induced accumulative processes leading to magnetization reversal in this particular material system. We used two different techniques to initialize the magnetization state between successive pump-probe cycles to experimentally work out the impact of the external magnetic field on the magnetization relaxation behavior. A permanently applied reset field always promotes the magnetization recovery and therefore obscures the intrinsic recovery effects. In contrast, magnetic state initialization by magnetic pulses between successive pump-probe cycles allows the system to relax by intrinsic processes governed by re-emerging exchange and anisotropy.

Our attempts to fit the experimental transient magnetization curves with extended three-temperature models show, especially for the E3TM, very good agreement for times up to 100 ps, but the thermal diffusion modeled in the E3TM and eM3TM by the K_l and τ_a terms, respectively, cannot reproduce the magnetization relaxation behavior beyond 200 ps, in particular its dependence on magnetic field and pump laser fluence (Appendix F). This unambiguous finding reveals that, in contrast to existing models, the relaxation dynamics beyond 100 ps is *not* governed by simple heat transfer from

the electron and spin systems into the heat reservoirs of the lattice and substrate.

In order to nonetheless analyze the recorded transients quantitatively, we adopted an approach similar to that used in previous phenomenological studies describing magneto-optical transients by constructing and applying a phenomenological response function. Our response function provides very good fits of the entire transients from femtosecond to nanosecond timescales using three phenomenological time constants, τ_m^*, τ_f^*, and τ_s^* (Figs. 3 and 4).

The analysis of the transient magnetization curves reveals that the applied magnetic field has little impact on short timescales below about 40 ps, but causes a magnetic field dependent speedup of the magnetization recovery for longer times, leading to decreasing τ_f^* and τ_s^* for increasing magnetic field (Fig. 3). The strongest difference between field-driven and intrinsic magnetization relaxation occurs after excitation at pump laser fluences that completely quench the sample magnetization. In this case, the system entirely loses the memory of the magnetic state before excitation, and recovery starts from random fluctuations, resulting in an extremely slow re-establishment of the magnetization. For large fluences, the totally quenched state can persist for more than 2 ns (Fig. 4) causing a 13-fold and 60-fold increase of τ_f^* and τ_s^*, respectively (Fig. 5). This long-lived quenched state may be the starting point of all-optical, single-pulse domain formation [17] and thus is also relevant for understanding the initial stages of accumulative all-optical magnetization switching [63,64].

A qualitative interpretation of the phenomenological time constants τ_f^* and τ_s^* in our response function can be given in the framework of the LLB model, where the recovery of the macroscopic magnetization requires that the individual local moments undergo both longitudinal and transverse relaxation. Longitudinal relaxation is associated with spin temperature cooling and occurs within few (type I) to tens (type II) of picoseconds, depending on the pump laser fluence and the resulting type of photoinduced spin dynamics. We phenomenologically ascribe τ_f^* to the longitudinal relaxation. In addition to restoring their *magnitude* by longitudinal relaxation, the local moments must also align in their *directions*. This transverse relaxation occurs via incoherent magnetization precession with Gilbert-type damping. The transverse relaxation is magnetic field dependent and proceeds on a timescale of nanoseconds. We interpretet τ_s^* as the time constant of the transverse relaxation.

The question of the completeness of the magnetic recovery after even longer times was addressed by recording so-called transient hysteresis loops after up to 5 ms after the excitation (Fig. 2 and Appendix D). We stress that these loops clearly reveal different timescales for the recovery of the transient saturation magnetization $m_S(t_d)$ and the transient coercive field $H_c'(t_d)$. While $m_S(t_d)$ recovers within 500 ps, $H_c'(t_d)$ has not entirely recovered even after 5 ms. Together, these two aspects suggest that the entire magnetic system evolves even on the millisecond timescale due to presence of transient metastable states. We attribute these metastable states to a few spatially small and pinned deviations from the ideal ferromagnetic ground state (e.g., small domains) due to rapid cooling and inhomogeneous temperature, magnetization, and magnetic anisotropy distributions.

Our results contribute to and advance the fundamental understanding of spin dynamics in ferromagnetic multilayers on various timescales relevant for spintronic applications such as MRAM, AOS, and THz generation.

Data and materials availability: All data needed to evaluate the conclusions in the paper are present in the paper and/or the Appendixes.

APPENDIX A: DETAILS ON PUMP-PROBE SETUP AND MEASUREMENT PROCEDURE

The pump probe experiments were carried out by using a combination of a fs-Tsunami as seed and a Spitfire laser as a regeneration amplifier system from Spectra Physics. The laser repetition rate can be tuned from 1-kHz to the Hz range. The pump-probe measurements were performed by first optically pumping the thin films with linearly polarized laser light with 800 nm wavelength and 80 fs duration. A comparably long probe pulse with 400 nm wavelength was generated by a 100-nm-thick BBO crystal via second harmonic generation. After interaction with the sample, the probe beam was reflected into a detection system. The beam passed first through a 400-nm band-pass filter and then a $\lambda/2$ plate for controlling the balance of the two orthogonal light components. With a Wollaston prism, the incoming beam was split into two orthogonally polarized beams, which were captured individually by a balanced pair of photodetectors detecting their light intensities A and B. After converting the light intensities to voltage signals, the two output signals were amplified and recorded as sum signal $A + B$ and difference signal $A - B$ by two separate Stanford-SR830 lock-in amplifiers, which were synchronized to the laser repetition frequency of 1 kHz (only some data in Fig. 9 have been measured with lower repetition frequencies of 200, 250, 333, and 500 Hz). Because the repetition frequency for lock-in synchronization is directly supplied by a dedicated photodiode placed inside a laser amplifier, a mechanical chopper is not essential for our setup. In addition, by dividing the difference of the two recorded signals by their sum, $(A-B)/(A+B)$, a possible long-term signal drift due to, e.g., a gradual warmup of the system or slowly changing laboratory environment during the day, can be efficiently eliminated from the magnetic contrast measurement. The final dynamic data were acquired by subtracting the transient magnetic contrasts measured at applied positive and negative magnetic field recorded with the smallest possible time difference, and no substantial signal drift has been detected in the respective traces.
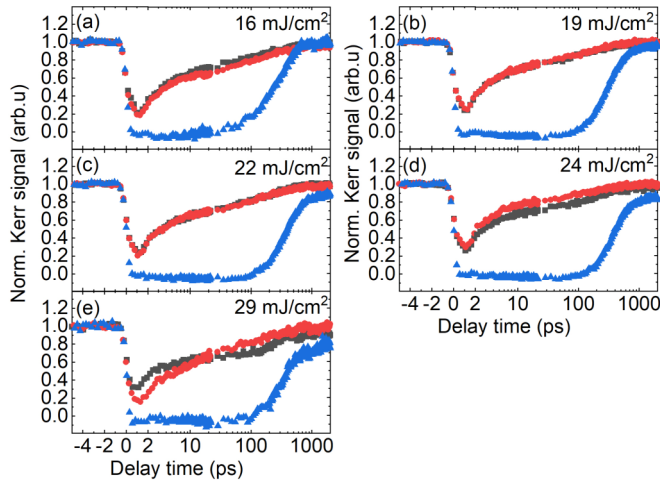
FIG. 7. TR-MOKE measurements at pristine positions with pump laser fluence variation in the sequence "low-high-low," where low fluence (red and black curves) was always 6 mJ/cm^2 and the high fluence (blue curves) is varied as indicated.

APPENDIX B: LASER FLUENCE THRESHOLD FOR SAMPLE MODIFICATION

Laser-induced permanent sample modification is an important issue in pump-probe experiments and must always be kept in mind, especially at high laser fluence. In order to stay below the threshold for sample damage, we have performed a set of measurements to ensure a safe range of the pump laser fluence (Fig. 7). On pristine sample positions, we measured TR-MOKE data at low and high pump laser fluence in the sequence of "low-high-low." The low fluence was always 6 mJ/cm^2, and the high fluence value was increased in five steps from 16 to 29 mJ/cm^2. The acquisition time for each transient is about 2 h. Our results show that the transient data measured under low pump fluence before and after recording the transient at high fluence are completely identical when the high fluence value is below 24 mJ/cm^2. All reported data in the paper are taken at laser fluences below 20 mJ/cm^2 and, thus, have a sufficient "safety margin" to the threshold for sample modification.

APPENDIX C: MEANING OF PARAMETERS A_1 AND A_2 IN OUR RESPONSE FUNCTION [EQ. (2)]

The phenomenological meaning of the parameters A_1 and A_2 in our response function [Eq. (2)] is best seen in Fig. 8, where we plot Eq. (2) for different A_2 values while keeping all other parameters constant. A_1 represents the normalized maximum amplitude of the laser-induced magnetization quenching that would be achieved in the absence of any relaxation (note, $A_1 = 1.0$ in Fig. 8). Hence, A_1 is mainly associated with the interaction of the pump light with the spin and electron systems. A_2 is a phenomenological measure of the strength of the relaxation slowdown. It indicates the remaining magnetization quenching level at the delay time, when, in the absence of relaxation slowdown (black curve for $A_2 = 0$), the subsystem temperatures would reach equilibrium and the normalized transient magnetization would return to saturation,
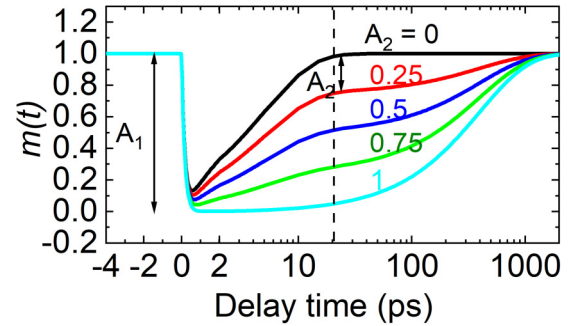
FIG. 8. Phenomenological response function [Eq. (2)] for different A_2 values as indicated. All other parameters are kept constant, $A_1 = 1.0$, $\tau_m^* = 160$ fs, $\tau_f^* = 5$ ps, and $\tau_s^* = 500$ ps. The dashed vertical line indicates the delay time, when the black curve for $A_2 = 0$, i.e., for no relaxation slowdown, reaches magnetization saturation.

$m(t) \approx 1$ (this time is marked by the vertical dashed line at $t \approx 20$ ps). For example, the red curve in Fig. 8 for $A_2 = 0.25$ is still quenched by about 25% at the delay time, when the black curve reaches magnetization saturation. τ_s^* determines the delay of the magnetization saturation, which occurs for $t \approx 4\tau_s^*$.

APPENDIX D: TRANSIENT HYSTERESIS LOOPS AS A FUNCTION OF LASER REPETITION RATE

To track magnetization relaxation after optical demagnetization for longer than 1 ms, we reduced the laser repetition rate for the measurement of transient hysteresis loops from 1 kHz to 200 Hz to achieve time intervals up to 5 ms between successive pump-probe cycles. Figure 9 shows that the transient hysteresis loops gradually recover and almost reach the shape of the static one at 3 ms pulse spacing. Small remaining differences between the transient and static coercive fields indicate that the relaxation processes may not be complete even 5 ms after sample excitation.
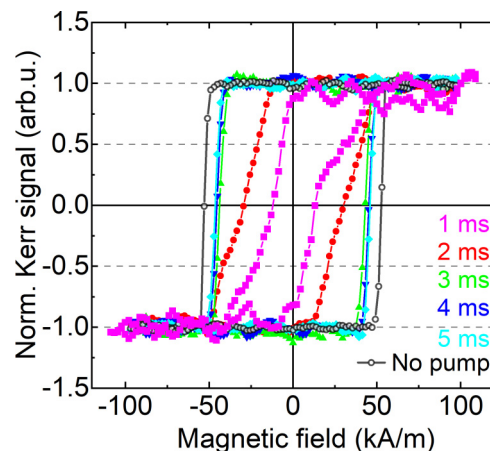
FIG. 9. Transient hysteresis loops at delay times of 1–5 ms in comparison with the static hysteresis (black curve).
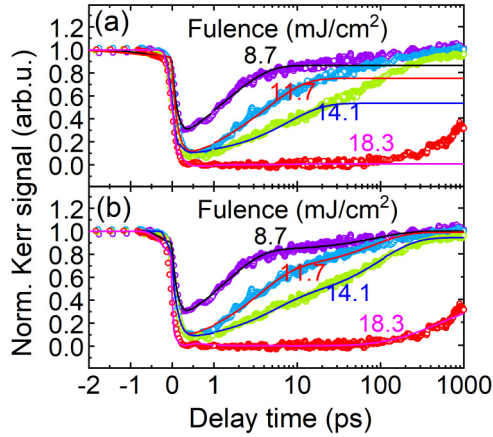
FIG. 10. Comparison of fit results obtained (a) with a phenomenological response function [Eq. (E1)] inspired by the analytical solution of the 2TM and (b) with our phenomenological response function [Eq. (E2)]. Our response function yields significantly improved fits for the delay times exceeding several tens of ps. The fitted data is a subset of the fluence dependent TR-P-MOKE measurements with pulsed magnetic state initialization presented in Fig. 4(b) of the main text.

APPENDIX E: DATA ANALYSIS USING PHENOMENOLOGICAL RESPONSE FUNCTIONS

For fitting the magnetization transient data, we first used a phenomenological response function

$$m(t) = G(t) \otimes [1 - \Theta(t - t_0)(A_1(1 - e^{-(t-t_0)/\tau_m})e^{-(t-t_0)/\tau_E}$$
$$+ A_2(1 - e^{-(t-t_0)/\tau_E}))] \tag{E1}$$

that is inspired by the analytical solution of the 2TM and has been frequently been employed to empirically describe sub-picosecond transient magnetization dynamics [30,48,49,51]. Using this equation, we consistently found substantial deviations between fitted and measured curves at the long timescale (>20 ps) with the deviations becoming larger with increasing pump laser fluence [Fig. 10(a)]. In order to improve the fits, we extended Eq. (E1) to obtain the following phenomenological response function, which we use for the fitting of all the experimental data:

$$m(t) = G(t) \otimes \{1 - \Theta(t - t_0)[A_1(1 - e^{-(t-t_0)/\tau_m^*})e^{-(t-t_0)/\tau_f^*}$$
$$+ A_2(1 - e^{-(t-t_0)/\tau_f^*})e^{-(t-t_0)/\tau_s^*}]\}. \tag{E2}$$

The main extension consists of multiplying an additional exponential term $e^{-(t-t_0)/\tau_s^*}$ to the second term of Eq. (E1), which introduces a third characteristic time τ_s^*. Since this extension

is purely phenomenological, we also replace τ_m and τ_E by *phenomenological* time constants τ_m^* and τ_f^*. We note that fitting measured transients with Eq. (E2) results in a substantial improvement of all fits [Fig. 10(b)]. The physical meaning of the extension is discussed in the main text.

In Tables I–III we compile all parameters that we extracted from our data by fitting $m(t)$ curves with our phenomenological response function given in Eq. (E2).

APPENDIX F: DATA ANALYSIS USING SOLUTIONS OF THE eM3TM AND THE E3TM

1. Fit results using the extended microscopic three-temperature model (eM3TM)

The eM3TM introduced by Bonda *et al.* [45] is an extension of the M3TM [27] that additionally accounts for the heat flow from the lattice system to the thermal reservoir of the substrate, which is considered as a thermostat at constant temperature T_a. To this end, a term is introduced in the set of differential equations of the eM3TM representing the cooling process of the lattice with a relaxation time τ_a to the ambient temperature T_a [see second term in Eq. (F1b)],

$$\frac{dT_e}{dt} = \frac{g_{el}(T_l - T_e)}{\gamma_e T_e} + \frac{P(t)}{\gamma_e T_e}, \tag{F1a}$$

$$\frac{dT_l}{dt} = \frac{g_{el}(T_e - T_l)}{C_l} + \frac{(T_a - T_l)}{\tau_a}, \tag{F1b}$$

$$\frac{dm}{dt} = Rm\frac{T_l}{T_C}\left[1 - m\coth\left(m\frac{T_C}{T_e}\right)\right], \tag{F1c}$$

$$\frac{dT_a}{dt} = 0, \tag{F1d}$$

where $P(t)$ is the Gaussian temporal profile of the pump laser pulse. T_e and T_l are the time dependent electronic and lattice temperature, respectively. $C_e = \gamma_e T_e$ and C_l represent the specific heat capacity of electronic and lattice subsystems, respectively, with g_{el} being the coupling parameter between the two subsystems. m is the time dependent normalized magnetization. T_C is the Curie temperature and R is a prefactor controlling the demagnetization rate [27] of the ferromagnetic material.

For the fitting procedure, $T_a = 300\,\text{K}$, $T_C = 600\,\text{K}$, and $C_l = 3.2 \times 10^6\,\text{J m}^{-3}\,\text{K}^{-1}$ is calculated as the mean value of the heat capacities of Co and Pt weighted by their volume ratio in the multilayer. The amplitude of $P(t)$ is calculated from the applied pump fluence and the laser pulse FWHM is fixed at 80 fs. The parameters $R = 4.8 \times 10^{-12}\,\text{s}^{-1}$ and $\gamma_e = 160\,\text{J m}^{-3}\,\text{K}^{-2}$ are also fixed constants and of the same

TABLE I. Dependence on the applied magnetic field presented in Fig. 3 of the main text.

H (kA/m)	A_1	A_2	τ_m^* (fs)	τ_f^* (ps)	τ_s^* (ns)
11.16	0.77 ± 0.04	0.57 ± 0.02	117.90 ± 13.66	10.12 ± 1.70	0.60 ± 0.06
23.11	0.89 ± 0.04	0.75 ± 0.03	165.79 ± 16.89	7.42 ± 1.96	0.47 ± 0.03
34.27	1.00 ± 0.07	0.83 ± 0.03	128.29 ± 12.78	8.68 ± 2.06	0.49 ± 0.04
45.43	1.00 ± 0.08	0.84 ± 0.03	173.31 ± 12.66	7.33 ± 1.56	0.37 ± 0.02
69.34	1.00 ± 0.11	0.84 ± 0.05	167.69 ± 14.16	5.93 ± 1.52	0.29 ± 0.02
90.86	1.00 ± 0.16	0.86 ± 0.04	150.64 ± 13.36	6.68 ± 1.55	0.23 ± 0.01

TABLE II. Dependence on laser fluence under magnetic state initialization with a constant magnetic field presented in Fig. 4(a) of the main text.

Fluence (mJ/cm^2)	A_1	A_2	τ_m^* (fs)	τ_f^* (ps)	τ_s^* (ns)
3.03	0.35 ± 0.05	0.06 ± 0.16	297.03 ± 545.85	0.58 ± 0.48	0.14 ± 0.06
6.03	0.50 ± 0.17	0.07 ± 0.12	93.87 ± 63.07	1.62 ± 0.49	0.16 ± 0.06
9.16	0.68 ± 0.16	0.28 ± 0.17	192.44 ± 32.82	2.71 ± 0.63	0.13 ± 0.01
11.83	0.82 ± 0.15	0.38 ± 0.13	154.77 ± 20.04	4.90 ± 0.29	0.15 ± 0.01
14.68	0.95 ± 0.13	0.65 ± 0.11	129.10 ± 25.87	5.07 ± 0.52	0.24 ± 0.02
19.06	1.06 ± 0.12	0.88 ± 0.06	188.27 ± 11.73	5.98 ± 0.70	0.29 ± 0.02

magnitudes as reported in [27] and [65], respectively. The other parameters, g_{el} and in particular τ_a are free parameters of the least-square fitting process. The results of fitting the eM3TM to our data are compiled in Fig. 11.

The fits for the field dependent data Fig. 11(a) show good agreement for short times (<100 ps) and external magnetic fields below 45 kA/m. For longer times and larger magnetic fields, we observe slight deviations from the experimental data. Stronger deviations are visible for the data measured in constant field [Fig. 11(b)] at short recovery times (≈ 1 ps) and low fluence, as also reported by Bonda *et al.* [45]. The strongest deviations occur for the data acquired with pulsed magnetic state initialization in Fig. 11(c) at various timescales and for all fluence values. All these deviations occur, even though we allowed τ_a to vary with magnetic field and fluence in a wide range [Figs. 11(d)–11(f)], which is a contradiction with the physical meaning of τ_a as the time constant describing heat flow between the system and the substrate. If τ_a is assumed constant, as suggested by the model assumption, the quality of the fits deteriorates on timescale exceeding 200 ps.

2. Fit result using extended three-temperature model (E3TM)

The E3TM introduced by Shim *et al.* [44] is an extension of the 3TM [1]. The main extension concerns the inclusion of the excitation of nonthermal electrons and the energy flow from the nonthermal electrons to the thermal electron, lattice, and spin subsystems. In addition and similar to the eM3TM, the E3TM also accounts for the heat flow from the lattice system to the thermal reservoir of the substrate, which is considered to be a thermostat at a constant temperature of 300 K. Here, this heat flow is formulated in terms of thermal diffusion, which is characterized by the coefficient K_l and is proportional to the

third power of temperature difference [66] [see the fourth term in Eq. (F2c)],

$$\frac{dN}{dt} = P(t) - P_e(t) - P_l(t) - P_s(t), \tag{F2a}$$

$$C_e \frac{dT_e}{dt} = P_e(t) - g_{el}(T_e - T_l) - g_{es}(T_e - T_s), \tag{F2b}$$

$$C_l \frac{dT_l}{dt} = P_l(t) - g_{el}(T_l - T_e) - g_{ls}(T_l - T_s) \\ - K_l(T_l - 300)^3, \tag{F2c}$$

$$C_s \frac{dT_s}{dt} = P_s(t) - g_{es}(T_s - T_e) - g_{ls}(T_s - T_l), \tag{F2d}$$

$$P_i(t) = \frac{g_{ei}}{C_e} N, \quad i = e, l, s. \tag{F2e}$$

Here, N is the optically pumped, nonthermal electron energy density, and $P(t)$ is the Gaussian temporal profile of the pump laser pulse. $P_e(t)$, $P_l(t)$, and $P_s(t)$ represent the energy flows from nonthermal electrons to the thermal electron, lattice, and spin systems, respectively. T_e, T_l, and T_s are the time dependent electronic, lattice, and spin temperature, respectively. $C_e = \gamma_e T_e$, C_l, and C_s represent the specific heat capacity of electron, lattice, and spin systems. g_{el}, g_{es}, and g_{ls}, are the coupling constant between electron and lattice, electron and spin, and lattice and spin subsystems, respectively. The time dependent normalized magnetization $m(t)$ is assumed to be proportional to the normalized solution for spin temperature $T_s(t)$.

For the fitting procedure, $T_C = 600\,\text{K}$ and $C_l = 3.2 \times 10^6\,\text{J m}^{-3}\,\text{K}^{-1}$ is calculated as the mean value of the heat capacities of Co and Pt weighted by their volume ratio in the multilayer. The amplitude of $P(t)$ is calculated from the applied pump fluence and the laser pulse FWHM is fixed at

TABLE III. Dependence on laser fluence under magnetic state initialization with a pulsed magnetic field presented in Fig. 4(b) of the main text.

Fluence (mJ/cm^2)	A_1	A_2	τ_m^* (fs)	τ_f^* (ps)	τ_s^* (ns)
8.71	0.66 ± 0.15	0.17 ± 0.14	180.06 ± 29.78	1.40 ± 0.14	0.09 ± 0.01
11.69	0.86 ± 0.24	0.33 ± 0.22	122.10 ± 13.79	3.34 ± 0.28	0.08 ± 0.01
13.49	0.94 ± 0.10	0.54 ± 0.05	121.30 ± 23.82	6.04 ± 0.43	0.10 ± 0.02
14.08	0.94 ± 0.06	0.51 ± 0.03	124.10 ± 32.58	4.55 ± 0.56	0.10 ± 0.02
14.93	0.98 ± 0.10	0.43 ± 0.06	123.62 ± 15.02	8.83 ± 1.53	0.16 ± 0.01
16.37	1.05 ± 0.14	0.56 ± 0.06	162.76 ± 25.99	9.32 ± 3.21	0.18 ± 0.02
18.31	1.01 ± 0.26	0.90 ± 0.26	120.59 ± 18.87	117.23 ± 18.36	13.33 ± 3.50
19.90	0.99 ± 0.25	0.95 ± 0.68	300.00 ± 107.60	120.00 ± 50.00	18.64 ± 3.65
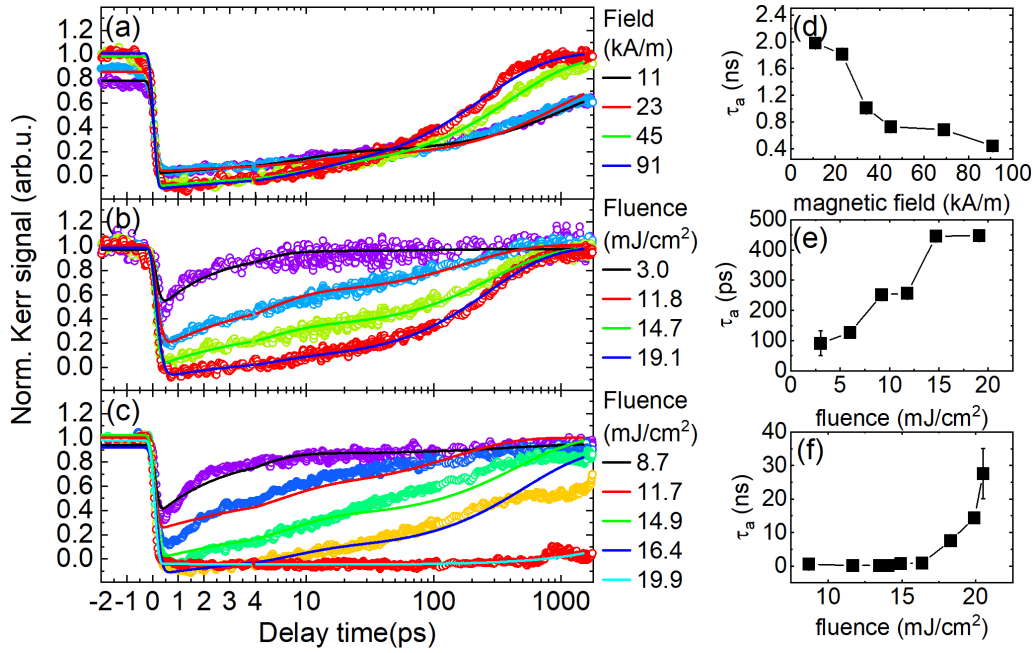
FIG. 11. Fitting results for the eM3TM. Solid lines are fits of TR-P-MOKE transients measured (a) as a function of permanent magnetic field [cf. Fig. 3(a)], (b) as a function of pump laser fluence with constant field magnetic state initialization [cf. Fig. 4(a)], and (c) as a function of pump laser fluence with pulsed field magnetic state initialization [cf. Fig. 4(b)]. (d) Magnetic field and (e),(f) fluence dependence of the time constant τ_a extracted from the fits in (a) and (b),(c) respectively.

80 fs. The parameters γ_e, g_{ee}, and g_{ls} are also fixed constants. $\gamma_e = 260 \, \mathrm{J \, m^{-3} \, K^{-2}}$ and $g_{ee} = 2.1 \times 10^{19} \, \mathrm{J \, s^{-1} \, m^{-3} \, K^{-1}}$ are of the same magnitudes as reported in [65] and [44], respectively, while $g_{ls} = 3.0 \times 10^{15} \, \mathrm{J \, s^{-1} \, m^{-3} \, K^{-1}}$ is about one order of magnitude smaller than in [46]. The other parameters, g_{el},

g_{es}, C_s, and in particular K_l, are free parameters of the least-square fitting process. The results of fitting the E3TM to our data are compiled in Fig. 12. We observe significant deviations of the fits from the data for all three measurement modes in Figs. 12(a)–12(c). In contrast to the fits to the eM3TM
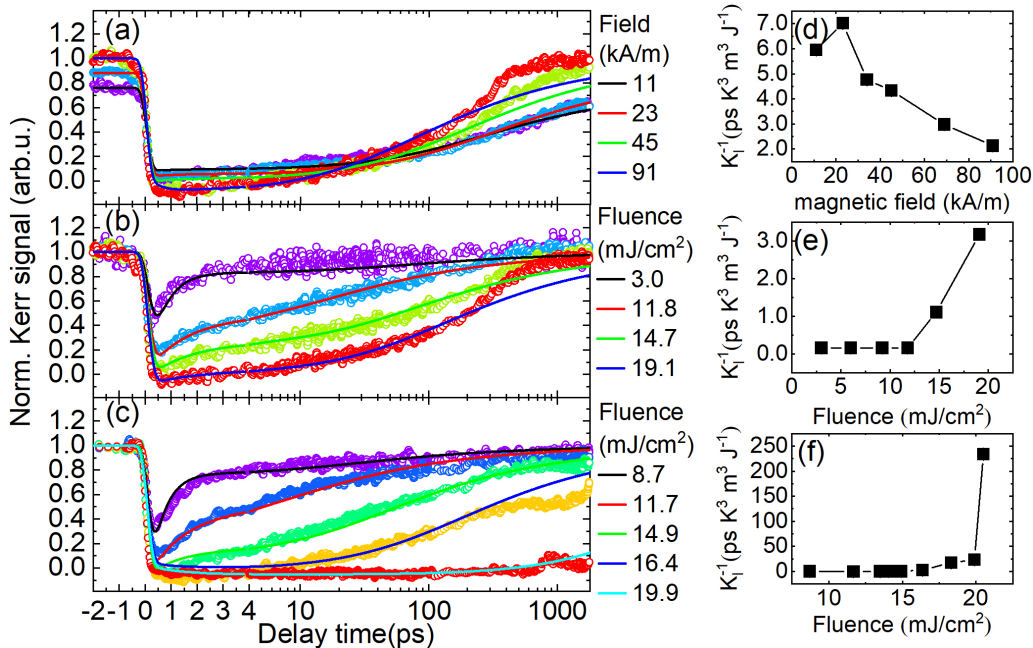
FIG. 12. Fitting results for the E3TM. Solid lines are fits of TR-P-MOKE transients measured (a) as a function of permanent magnetic field [cf. Fig. 3(a)], (b) as a function of pump laser fluence with constant field magnetic state initialization [cf. Fig. 4(a)], and (c) as a function of pump laser fluence with pulsed field magnetic state initialization [cf. Fig. 4(b)]. (d) Magnetic field and (e),(f) fluence dependence of the inverse thermal diffusion coefficient K_l^{-1} extracted from the fits shown in (a) and (b),(c) respectively.
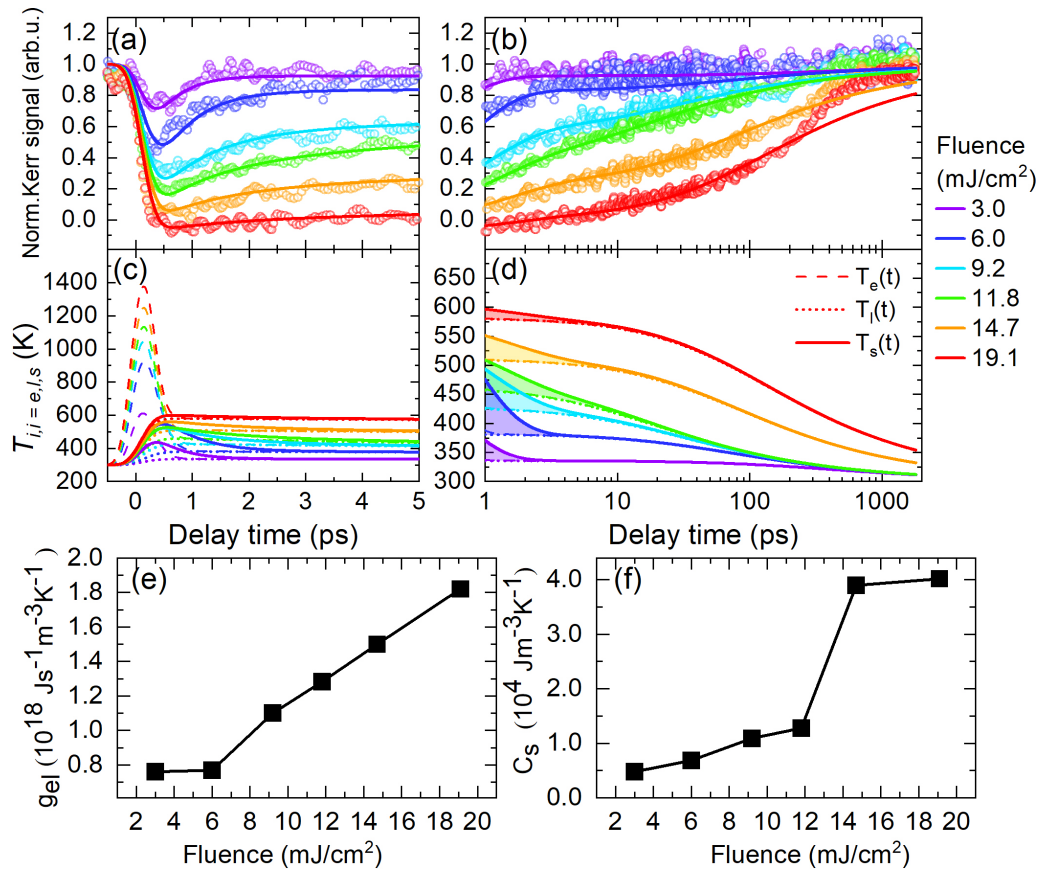
FIG. 13. Fitting results for the E3TM. Solid lines in (a) and (b) are fits of TR-P-MOKE transients measured as a function of pump laser fluence with constant field magnetic state initialization [cf. Fig. 4(a)]. Panel (a) shows delay times up to 5 ps on a linear time axis and (b) delay times up 2 ns on a logarithmic timescale. Panels (c) and (d) show the corresponding evolutions of $T_e(t)$, $T_l(t)$, and $T_s(t)$ on (c) short and (d) long timescales marked as solid, dashed, and dotted and solid lines, respectively. Colored areas in (d) indicate time intervals, where $T_s(t)$ exceeds $T_e(t)$ and $T_l(t)$. Panels (e) and (f) show the fluence dependence of (e) the electron-lattice coupling constant g_{el} and (f) the spin specific heat capacity C_s.

(Fig. 11), the deviations are more systematic. They occur for long times scales (>200 ps) and are more pronounced at larger magnetic field [Fig. 12(a)] or larger pump laser fluence [Figs. 12(b) and 12(c)].

Figure 13 shows further details of the fitting with the E3TM using the example of the fluence dependent magnetization transients measured with constant field magnetic state initialization [cf. Fig. 4(a)]. Figure 13(a) shows fits (solid lines) and experimental data (symbols) for short delay times (<5 ps) on a linear timescale and Fig. 13(b) for longer delay times on a logarithmic timescale. With increasing fluence, there is a gradual transition from relaxation within a few ps (type I) to slowed down relaxation on the 100 ps to nanosecond timescale (type II). The evolution of the temperatures $T_e(t)$, $T_l(t)$, and $T_s(t)$ on short and long timescales is displayed in Figs. 13(c) and 13(d) by as dashed, dotted, and solid lines, respectively. Note in Fig. 13(d) that in the colored regions the spin temperature $T_s(t)$ exceeds the electron and lattice temperatures $T_e(t)$ and $T_l(t)$, which are already in equilibrium with each other (dashed and doted curves are superimposed). Both effects, type-I to type-II transition and delayed equilibration of $T_s(t)$ have been shown by Shim *et al.* [44] to be related to the energy flow from nonthermal electrons to the thermal electron, spin, and lattice subsystems. The fit results

reveal that the electron-lattice coupling constant g_{el} features the strongest dependence on the pump laser fluence among all coupling constants (g_{el}, g_{es}, g_{ls}, and g_{ee}); see Fig. 13(e). Furthermore, the specific capacity of the spin subsystem C_s shown in Fig. 13(f) increases abruptly for pump laser fluences above 14 mJ/cm², for which the maximum spin temperature approaches the Curie temperature of the Co/Pt multilayer ($T_C \approx 600$ K). This is in excellent agreement with the expectation that $C_s(T_s)$ peaks at the second order phase transition occurring at T_C. Despite these agreements, for delay times exceeding 200 ps, as shown in Fig. 13(b), varying degrees of discrepancy between data and fits occur as a function of fluence at different delay times. The stronger the fluence, the larger the deviation and the earlier the deviation appears, as already observed in Figs. 12(b) and 12(c).

In addition, we stress again that the observed deviations in Figs. 12 and 13 occur although we allowed K_l to vary with magnetic field and pump laser fluence; see Figs. 12(d)–12(f). While these allowed strong variations improve the fits, they are in contradiction with the physical meaning of K_l as the thermal heat diffusion coefficient describing heat flow between the system and the substrate. If K_l is assumed constant, as suggested by the model assumption, the quality of the fits deteriorates on timescales exceeding 200 ps.

TABLE IV. The parameters used for the E3TM calculations in Fig. 6(a).

Parameter	Type I (6 mJ/cm²)	Type II (19.1 mJ/cm²)	Remark
$P(t)$ amplitude	0.6×10^9 J m^{-3}	1.9×10^9 J m^{-3}	Calculated from fluence
$P(t)$ FWHM	80 fs	80 fs	Fixed
C_l	3.3×10^6 J m^{-3} K^{-1}	3.3×10^6 J m^{-3} K^{-1}	Mean value of Co and Pt, weighted by volume ratio
C_s	6.8×10^3 J m^{-3} K^{-1}	0.4×10^3 J m^{-3} K^{-1}	Fitted [see Fig. 4(a)]
γ_e	2.6×10^2 J m^{-3} K^{-2}	2.6×10^2 J m^{-3} K^{-2}	Same magnitude as in [65]
g_{el}	0.8×10^{18} J s^{-1} m^{-3} K^{-1}	1.9×10^{18} J s^{-1} m^{-3} K^{-1}	Fitted [see Fig. 4(a)]
g_{es}	0.8×10^{16} J s^{-1} m^{-3} K^{-1}	2.4×10^{17} J s^{-1} m^{-3} K^{-1}	Fitted [see Fig. 4(a)]
g_{ls}	3.0×10^{15} J s^{-1} m^{-3} K^{-1}	3.0×10^{15} J s^{-1} m^{-3} K^{-1}	About one order of magnitude smaller than in [46]
g_{ee}	2.1×10^{19} J s^{-1} m^{-3} K^{-1}	2.1×10^{19} J s^{-1} m^{-3} K^{-1}	Same magnitude as in [44]
K_l	6.3×10^{12} J s^{-1} m^{-3} K^{-3}	0.3×10^{12} J s^{-1} m^{-3} K^{-3}	Fitted [see Fig. 4(a)]

Comparison of the eM3TM and E3TM results shows that the E3TM provides better fits for short delay times (<200 ps). But both models seem to overlook a magnetic field and fluence dependent mechanism that is effective on longer timescales, as evidenced not only by the observed fitting deviations, but also by the systematic but unphysical field and fluence dependencies of τ_a and K_l. Due to this lack of a model that allows fitting the fluence and field dependence of the relaxation behavior on long timescales, we were compelled to introduce the additional phenomenological time constant τ_s^*. In the main text,

we provide an interpretation of τ_s^* in the framework of LLB-like transverse magnetization relaxation, which is intrinsically magnetic field dependent.

APPENDIX G: PARAMETERS FOR THE E3TM CALCULATIONS IN FIG. 6(a)

See Table IV for parameters used for the E3TM calculations in Fig. 6(a).

[1] E. Beaurepaire, J. C. Merle, A. Daunois, and J. Y. Bigot, Ultrafast Spin Dynamics in Ferromagnetic Nickel, Phys. Rev. Lett. **76**, 4250 (1996).

[2] A. Kirilyuk, A. V. Kimel, and T. Rasing, Ultrafast optical manipulation of magnetic order, Rev. Mod. Phys. **82**, 2731 (2010).

[3] A. V. Kimel and M. Li, Writing magnetic memory with ultrashort light pulses, Nat. Rev. Mater. **4**, 189 (2019).

[4] J.-Y. Chen, L. He, J.-P. Wang, and M. Li, All-Optical Switching of Magnetic Tunnel Junctions with Single Subpicosecond Laser Pulses, Phys. Rev. Appl. **7**, 021001(R) (2017).

[5] S. A. Wolf, D. D. Awschalom, R. A. Buhrman, J. M. Daughton, S. von Molnár, M. L. Roukes, A. Y. Chtchelkanova, and D. M. Treger, Spintronics: A spin-based electronics vision for the future, Science **294**, 1488 (2001).

[6] C. Chappert, A. Fert, and F. N. Van Dau, The emergence of spin electronics in data storage, Nat. Mater. **6**, 813 (2007).

[7] K. Vahaplar, A. M. Kalashnikova, A. V. Kimel, D. Hinzke, U. Nowak, R. Chantrell, A. Tsukamoto, A. Itoh, A. Kirilyuk, and T. Rasing, Ultrafast Path for Optical Magnetization Reversal via a Strongly Nonequilibrium State, Phys. Rev. Lett. **103**, 117201 (2009).

[8] C. D. Stanciu, F. Hansteen, A. V. Kimel, A. Kirilyuk, A. Tsukamoto, A. Itoh, and T. Rasing, All-Optical Magnetic Recording with Circularly Polarized Light, Phys. Rev. Lett. **99**, 047601 (2007).

[9] I. Radu, K. Vahaplar, C. Stamm, T. Kachel, N. Pontius, H. A. Dürr, T. A. Ostler, J. Barker, R. F. L. Evans, R. W. Chantrell *et al.*, Transient ferromagnetic-like state mediating ultrafast reversal of antiferromagnetically coupled spins, Nature (London) **472**, 205 (2011).

[10] T. A. Ostler, J. Barker, R. F. L. Evans, R. W. Chantrell, U. Atxitia, O. Chubykalo-Fesenko, S. El Moussaoui, L. Le Guyader, E. Mengotti, L. J. Heyderman *et al.*, Ultrafast heating as a sufficient stimulus for magnetization reversal in a ferrimagnet, Nat. Commun. **3**, 666 (2012).

[11] G. Kichin, M. Hehn, J. Gorchon, G. Malinowski, J. Hohlfeld, and S. Mangin, From Multiple- to Single-Pulse All-Optical Helicity-Dependent Switching in Ferromagnetic Co/Pt Multilayers, Phys. Rev. Appl. **12**, 024019 (2019).

[12] S. Alebrand, A. Hassdenteufel, D. Steil, M. Bader, A. Fischer, M. Cinchetti, and M. Aeschlimann, All-optical magnetization switching using phase shaped ultrashort laser pulses, Phys. Status Solidi A **209**, 2589 (2012).

[13] C. H. Lambert, S. Mangin, B. Varaprasad, Y. K. Takahashi, M. Hehn, M. Cinchetti, G. Malinowski, K. Hono, Y. Fainman, M. Aeschlimann *et al.*, All-optical control of ferromagnetic thin films and nanostructures, Science **345**, 1337 (2014).

[14] N. Bergeard, M. Hehn, S. Mangin, G. Lengaigne, F. Montaigne, M. L. M. Lalieu, B. Koopmans, and G. Malinowski, Hot-Electron-Induced Ultrafast Demagnetization in Co/Pt Multilayers, Phys. Rev. Lett. **117**, 147203 (2016).

[15] W. B. Zeper, F. J. A. M. Greidanus, P. F. Carcia, and C. R. Fincher, Perpendicular magnetic anisotropy and magneto-optical Kerr effect of vapor-deposited Co/Pt-layered structures, J. Appl. Phys. **65**, 4971 (1989).

[16] S. Hashimoto, Y. Ochiai, and K. Aso, Film thickness dependence of magneto-optical and magnetic properties in Co/Pt and Co/Pd multilayers, J. Appl. Phys. **67**, 4429 (1990).

[17] U. Parlak, R. Adam, D. E. Bürgler, S. Gang, and C. M. Schneider, Optically induced magnetization reversal in [Co/Pt]$_N$ multilayers: Role of domain wall dynamics, Phys. Rev. B **98**, 214443 (2018).

[18] F. Garcia, F. Fettar, S. Auffret, B. Rodmacq, and B. Dieny, Exchange-biased spin valves with perpendicular magnetic anisotropy based on (Co/Pt) multilayers, J. Appl. Phys. **93**, 8397 (2003).

[19] P. Matthes, S. S. P. K. Arekapudi, F. Timmermann, and M. Albrecht, Magnetotransport properties of perpendicular [Pt/Co]/Cu/[Co/Pt] pseudo-spin-valves, IEEE Trans. Magn. **51**, 1 (2015).

[20] Z. Kugler, J.-P. Grote, V. Drewello, O. Schebaum, G. Reiss, and A. Thomas, Co/Pt multilayer-based magnetic tunnel junctions with perpendicular magnetic anisotropy, J. Appl. Phys. **111**, 07C703 (2012).

[21] J.-H. Park, C. Park, T. Jeong, M. T. Moneck, N. T. Nufer, and J.-G. Zhu, Co/Pt multilayer based magnetic tunnel junctions using perpendicular magnetic anisotropy, J. Appl. Phys. **103**, 07A917 (2008).

[22] R. Sbiaa, H. Meng, and S. N. Piramanayagam, Materials with perpendicular magnetic anisotropy for magnetic random access memory, Phys. Status Solidi RRL **5**, 413 (2011).

[23] S. Woo, K. Litzius, B. Krger, M.-Y. Im, L. Caretta, K. Richter, M. Mann, A. Krone, R. M. Reeve, M. Weigand *et al.*, Observation of room-temperature magnetic skyrmions and their current-driven dynamics in ultrathin metallic ferromagnets, Nat. Mater. **15**, 501 (2016).

[24] G. Li, R. Medapalli, R. V. Mikhaylovskiy, F. E. Spada, T. Rasing, E. E. Fullerton, and A. V. Kimel, THz emission from Co/Pt bilayers with varied roughness, crystal structure, and interface intermixing, Phys. Rev. Mater. **3**, 084415 (2019).

[25] T. J. Huisman, R. V. Mikhaylovskiy, J. D. Costa, F. Freimuth, E. Paz, J. Ventura, P. P. Freitas, S. Blügel, Y. Mokrousov, T. Rasing *et al.*, Femtosecond control of electric currents in metallic ferromagnetic heterostructures, Nat. Nanotechnol. **11**, 455 (2016).

[26] M. v. Kampen, J. T. Kohlhepp, W. J. M. d. Jonge, B. Koopmans, and R. Coehoorn, Sub-picosecond electron and phonon dynamics in nickel, J. Phys.: Condens. Matter **17**, 6823 (2005).

[27] B. Koopmans, G. Malinowski, F. Dalla Longa, D. Steiauf, M. Fähnle, T. Roth, M. Cinchetti, and M. Aeschlimann, Explaining the paradoxical diversity of ultrafast laser-induced demagnetization, Nat. Mater. **9**, 259 (2009).

[28] N. Moisan, G. Malinowski, J. Mauchain, M. Hehn, B. Vodungbo, J. Lüning, S. Mangin, E. E. Fullerton, and A. Thiaville, Investigating the role of superdiffusive currents in laser induced demagnetization of ferromagnets with nanoscale magnetic domains, Sci. Rep. **4**, 4658 (2014).

[29] U. Bierbrauer, S. T. Weber, D. Schummer, M. Barkowski, A.-K. Mahro, S. Mathias, H. Christian Schneider, B. Stadtmller, M. Aeschlimann, and B. Rethfeld, Ultrafast magnetization dynamics in Nickel: Impact of pump photon energy, J. Phys.: Condens. Matter **29**, 244002 (2017).

[30] B. Vodungbo, J. Gautier, G. Lambert, A. B. Sardinha, M. Lozano, S. Sebban, M. Ducousso, W. Boutu, K. Li, B. Tudu *et al.*, Laser-induced ultrafast demagnetization in the presence of a nanoscale magnetic domain network, Nat. Commun. **3**, 999 (2012).

[31] G. Ju, A. Vertikov, A. V. Nurmikko, C. Canady, G. Xiao, R. F. C. Farrow, and A. Cebollada, Ultrafast nonequilibrium spin dynamics in a ferromagnetic thin film, Phys. Rev. B **57**, R700 (1998).

[32] D. A. Garanin, Fokker-Planck and landau-lifshitz-bloch equations for classical ferromagnets, Phys. Rev. B **55**, 3050 (1997).

[33] U. Atxitia and O. Chubykalo-Fesenko, Ultrafast magnetization dynamics rates within the landau-lifshitz-bloch model, Phys. Rev. B **84**, 144414 (2011).

[34] U. Atxitia, O. Chubykalo-Fesenko, N. Kazantseva, D. Hinzke, U. Nowak, and R. W. Chantrell, Micromagnetic modeling of laser-induced magnetization dynamics using the landau-lifshitz-bloch equation, Appl. Phys. Lett. **91**, 232507 (2007).

[35] U. Atxitia, O. Chubykalo-Fesenko, J. Walowski, A. Mann, and M. Münzenberg, Evidence for thermal mechanisms in laser-induced femtosecond spin dynamics, Phys. Rev. B **81**, 174401 (2010).

[36] A. Barman, S. Wang, O. Hellwig, A. Berger, E. E. Fullerton, and H. Schmidt, Ultrafast magnetization dynamics in high perpendicular anisotropy Co/Pt (n) multilayers, J. Appl. Phys. **101**, 09D102 (2007).

[37] A. Bonda, S. Uba, L. Uba, W. Skowroński, T. Stobiecki, and F. Stobiecki, Laser-induced magnetization precession parameters dependence on Pt spacer layer thickness in mixed magnetic anisotropies Co/Pt/Co trilayer, J. Magn. Magn. Mater. **505**, 166702 (2020).

[38] Y. Tsema, G. Kichin, O. Hellwig, V. Mehta, A. V. Kimel, A. Kirilyuk, and T. Rasing, Helicity and field dependent magnetization dynamics of ferromagnetic Co/Pt multilayers, Appl. Phys. Lett. **109**, 072405 (2016).

[39] C. La-O-Vorakiat, E. Turgut, C. A. Teale, H. C. Kapteyn, M. M. Murnane, S. Mathias, M. Aeschlimann, C. M. Schneider, J. M. Shaw, H. T. Nembach *et al.*, Ultrafast Demagnetization Measurements Using Extreme Ultraviolet Light: Comparison of Electronic and Magnetic Contributions, Phys. Rev. X **2**, 011005 (2012).

[40] D. Afanasiev, I. Razdolski, K. M. Skibinsky, D. Bolotin, S. V. Yagupov, M. B. Strugatsky, A. Kirilyuk, T. Rasing, and A. V. Kimel, Laser Excitation of Lattice-Driven Anharmonic Magnetization Dynamics in Dielectric FeBO_3, Phys. Rev. Lett. **112**, 147403 (2014).

[41] A. B. Schmidt, M. Pickel, M. Donath, P. Buczek, A. Ernst, V. P. Zhukov, P. M. Echenique, L. M. Sandratskii, E. V. Chulkov, and M. Weinelt, Ultrafast Magnon Generation in an Fe Film on Cu(100), Phys. Rev. Lett. **105**, 197401 (2010).

[42] T. D. Cornelissen, R. Cordoba, and B. Koopmans, Microscopic model for all optical switching in ferromagnets, Appl. Phys. Lett. **108**, 142405 (2016).

[43] J. Gorchon, Y. Yang, and J. Bokor, Model for multishot all-thermal all-optical switching in ferromagnets, Phys. Rev. B **94**, 020409(R) (2016).

[44] J.-H. Shim, A. A. Syed, J.-I. Kim, H.-G. Piao, S.-H. Lee, S.-Y. Park, Y. S. Choi, K. M. Lee, H.-J. Kim, J.-R. Jeong *et al.*, Role of non-thermal electrons in ultrafast spin dynamics of ferromagnetic multilayer, Sci. Rep. **10**, 6355 (2020).

[45] A. Bonda, L. Uba, K. Zaleski, and S. Uba, Ultrafast magnetization dynamics in an epitaxial NiMnSn heusler-alloy film close to the curie temperature, Phys. Rev. B **99**, 184424 (2019).

[46] J.-H. Shim, A. Ali Syed, C.-H. Kim, K. M. Lee, S.-Y. Park, J.-R. Jeong, D.-H. Kim, and D. Eon Kim, Ultrafast giant magnetic cooling effect in ferromagnetic Co/Pt multilayers, Nat. Commun. **8**, 796 (2017).

[47] S. Mathias, C. La-o-vorakiat, J. M. Shaw, E. Turgut, P. Grychtol, R. Adam, D. Rudolf, H. T. Nembach, T. J. Silva, M. Aeschlimann *et al.*, Ultrafast element-specific magnetiza-

tion dynamics of complex magnetic materials on a table-top, J. Electron Spectrosc. Relat. Phenom. **189**, 164 (2013).

[48] V. Cardin, T. Balciunas, K. Légaré, A. Baltuska, H. Ibrahim, E. Jal, B. Vodungbo, N. Jaouen, C. Varin, J. Lüning *et al.*, Wavelength scaling of ultrafast demagnetization in Co/Pt multilayers, Phys. Rev. B **101**, 054430 (2020).

[49] N. Del Fatti, C. Voisin, M. Achermann, S. Tzortzakis, D. Christofilos, and F. Vallée, Nonequilibrium electron dynamics in noble metals, Phys. Rev. B **61**, 16956 (2000).

[50] L. Guidoni, E. Beaurepaire, and J.-Y. Bigot, Magneto-optics in the Ultrafast Regime: Thermalization of Spin Populations in Ferromagnetic Films, Phys. Rev. Lett. **89**, 017401 (2002).

[51] A. Labourt-Ibarre, C. Voisin, G. Cassabois, C. Delalande, C. Flytzanis, P. Roussignol, and P. Beauvillain, Ultrafast electron thermalization in a magnetic layered Au/Co/Au film, J. Appl. Phys. **104**, 094301 (2008).

[52] C. Boeglin, E. Beaurepaire, V. Halté, V. López-Flores, C. Stamm, N. Pontius, H. A. Dürr, and J. Y. Bigot, Distinguishing the ultrafast dynamics of spin and orbital moments in solids, Nature (London) **465**, 458 (2010).

[53] B. Pfau, S. Schaffert, L. Müller, C. Gutt, A. Al-Shemmary, F. Büttner, R. Delaunay, S. Düsterer, S. Flewett, R. Frömter *et al.*, Ultrafast optical demagnetization manipulates nanoscale spin structure in domain walls, Nat. Commun. **3**, 1100 (2012).

[54] K. Yamamoto, S. E. Moussaoui, Y. Hirata, S. Yamamoto, Y. Kubota, S. Owada, M. Yabashi, T. Seki, K. Takanashi, I. Matsuda *et al.*, Element-selectively tracking ultrafast demagnetization process in Co/Pt multilayer thin films by the resonant magneto-optical Kerr effect, Appl. Phys. Lett. **116**, 172406 (2020).

[55] F. Dalla Longa, J. T. Kohlhepp, W. J. M. de Jonge, and B. Koopmans, Influence of photon angular momentum on ultrafast demagnetization in nickel, Phys. Rev. B **75**, 224431 (2007).

[56] Y. G. Gurevich, G. N. Logvinov, A. F. Carballo-Sanchez, Y. V. Drogobitskiy, and J. L. Salazar, Electron and phonon tem-perature relaxation in semiconductors excited by thermal pulse, J. Appl. Phys. **91**, 183 (2001).

[57] J. Kimling, J. Kimling, R. B. Wilson, B. Hebler, M. Albrecht, and D. G. Cahill, Ultrafast demagnetization of FePt:Cu thin films and the role of magnetic heat capacity, Phys. Rev. B **90**, 224408 (2014).

[58] D. Weller, Y. Wu, J. Stöhr, M. G. Samant, B. D. Hermsmeier, and C. Chappert, Orbital magnetic moments of Co in multilayers with perpendicular magnetic anisotropy, Phys. Rev. B **49**, 12888 (1994).

[59] M. T. Islam, X. S. Wang, and X. R. Wang, Thermal gradient driven domain wall dynamics, J. Phys.: Condens. Matter **31**, 455701 (2019).

[60] J. Chico, C. Etz, L. Bergqvist, O. Eriksson, J. Fransson, A. Delin, and A. Bergman, Thermally driven domain-wall motion in Fe on W(110), Phys. Rev. B **90**, 014434 (2014).

[61] Y. J. Chen, K. Zakeri, A. Ernst, H. J. Qin, Y. Meng, and J. Kirschner, Group Velocity Engineering of Confined Ultrafast Magnons, Phys. Rev. Lett. **119**, 267201 (2017).

[62] E. S. Demidov, N. S. Gusev, L. I. Budarin, E. A. Karashtin, V. L. Mironov, and A. A. Fraerman, Interlayer interaction in multilayer [Co/Pt]n/Pt/Co structures, J. Appl. Phys. **120**, 173901 (2016).

[63] Y. Quessab, R. Medapalli, M. S. El Hadri, M. Hehn, G. Malinowski, E. E. Fullerton, and S. Mangin, Helicity-dependent all-optical domain wall motion in ferromagnetic thin films, Phys. Rev. B **97**, 054419 (2018).

[64] M. S. El Hadri, M. Hehn, G. Malinowski, and S. Mangin, Materials and devices for all-optical helicity-dependent switching, J. Phys. D: Appl. Phys. **50**, 133002 (2017).

[65] R. J. Corruccini and J. J. Gniewek, *Specific Heat and Enthalpies of Technical Solids at Low Temperatures*, (National Bureau of Standards, Washington D.C., 1960).

[66] J. Liao, P. Gao, L. Xu, and J. Feng, A study of morphological properties of SiO2 aerogels obtained at different temperatures, J. Adv. Ceram. **7**, 307 (2018).